Acta Materialia

Strong and Ductile Refractory High-Entropy Alloys with Super Formability

--Manuscript Draft--

Manuscript Number:	A-22-1972R1
Article Type:	Full length article
Keywords:	Refractory high-entropy alloys; formability; cryogenic-to-elevated temperatures; Strength-ductility synergy
Corresponding Author:	Enrique Lavernia, PhD University of California, Irvine Irvine, California UNITED STATES
First Author:	Cheng Zhang, Ph.D
Order of Authors:	Cheng Zhang, Ph.D
	Haoren Wang, Ph.D
	Xinyi Wang, Ph.D
	Yuanbo T. Tang, Ph.D
	Qin Yu, Ph.D
	Chaoyi Zhu, Ph.D
	Mingjie Xu, Ph.D
	Shiteng Zhao, Ph.D
	Rui Kou, Ph.D
	Xin Wang, Ph.D
	Benjamin E. MacDonald, Ph.D
	Roger C. Reed, Ph.D
	Kenneth S. Vecchio, Ph.D
	Penghui Cao, Ph.D
	Timothy J. Rupert, Ph.D
	Enrique J. Lavernia, Ph.D
Abstract:	Refractory high-entropy alloys (RHEAs) are considered promising candidate materials for high-temperature structural applications that currently use superalloys. However, for most of the reported RHEAs, their poor ductility and negligible cold-workability at room temperature have hindered their use. Here, we report a new class of non-equiatomic NbTaTi-based RHEAs that can be cold-rolled to a reduction of over 90% from the as-cast state without surface treatment and/or intermediate annealing. This excellent cold-workability is facilitated by activation of a high-density of dislocations and deformation twins as well as by high diffusivity paths, such that these RHEAs can be rendered homogeneous at lower annealing temperatures for much shorter time durations. In addition, we report that the RHEAs retain their high strength at elevated temperatures and exhibit considerable ductility at cryogenic conditions, evading the traditional strength–ductility trade-off. This class of super-formable RHEAs provides a novel design pathway to fabricate high-temperature structural materials via an energy- and time-saving method.

Letter in Response to Reviewer Comments: A-22-1922

We appreciate the comments and suggestions from the two anonymous reviewers regarding our submission: “Strong and Ductile Refractory High-Entropy Alloys with Super Formability”. We revised our manuscript in response to their comments and below we provide detailed responses to each of the reviewers’ comments.

The reviewers’ comments are presented below, separated by *********, with our detailed response following and highlighted in grey. Kindly note that the revised manuscript has been revised (and highlighted in yellow) to reflect all of the changes where appropriate.

Reviewer #1: In this manuscript, the authors have demonstrated the microstructure and mechanical response of Nb-25Ta-15Ti-based RHEA over a wide range of temperatures. After heavy cold-rolled and the following annealing, the mechanical properties of the RHEA are improved obviously. However, aspects of the discussion are difficult to support the observed results with confidence, in particular, the discussions of the microstructure evolution. Hence, before consideration for acceptance, the questions listed below must properly addressed.

We thank the reviewer for the above comments.

****

1. First of all, the article data is incomplete and lacks supplementary information. The authors did not submit complete supplementary data, which makes the paper difficult to read and the conclusions of the paper unconvincing. Authors need to provide supplementary data to complete the structure of the article.

Thank you for these comments. During the submission process, we uploaded the supplementary information as a PDF document (13 figures and 2 tables) in the online system following publisher’s instructions. After submission, we confirmed that the PDF document can be downloaded (“Click here to access/download Supplementary Material”), as shown in the following figure (Fig. R1). We are not certain as to the reason why the reviewer did not see the submitted supplementary information. To make sure the reviewer can access to the file, we added all the original supplementary material to this document.

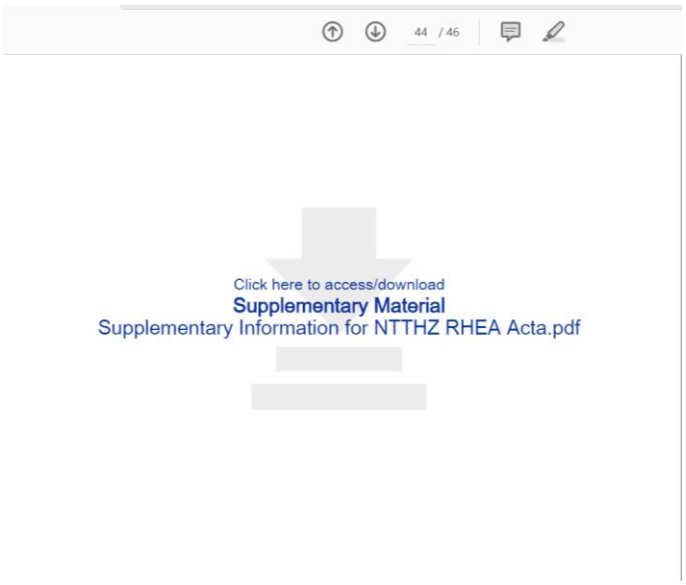

Fig. R1 Figure of uploaded “Supplementary Material” page.

Supplementary Information

Strong and Ductile Refractory High-Entropy Alloys with Super Formability

Authors: Cheng Zhang[1], Haoren Wang[2], Xinyi Wang[3], Yuanbo T. Tang[4], Qin Yu[5,6], Chaoyi Zhu[6], Mingjie Xu[1], Shiteng Zhao[6], Rui Kou[7], Xin Wang[1], Benjamin E. MacDonald[1], Roger C. Reed[4], Kenneth S. Vecchio[2], Penghui Cao[3], Timothy J. Rupert[1], Enrique J. Lavernia[1,*]

Affiliations:
[1] Department of Materials Science and Engineering, University of California Irvine, Irvine, CA 92697, USA
[2] Department of NanoEngineering, University of California San Diego, La Jolla, CA 92093, USA
[3] Department of Mechanical and Aerospace Engineering, University of California Irvine, Irvine, CA 92697, USA
[4] Department of Materials, University of Oxford, Parks Road, Oxford, OX1 3PH, United Kingdom
[5] Materials Sciences Division, Lawrence Berkeley National Laboratory, Berkeley, CA 94720, USA
[6] Department of Materials Science and Engineering, University of California, Berkeley, CA 94720, USA
[7] Department of Structural Engineering, UC San Diego, La Jolla, CA 92093, USA

*Corresponding author. Email: lavernia@uci.edu

This PDF file includes:

1. Supplementary Figs. 1-13
2. Supplementary Table 1 and 2

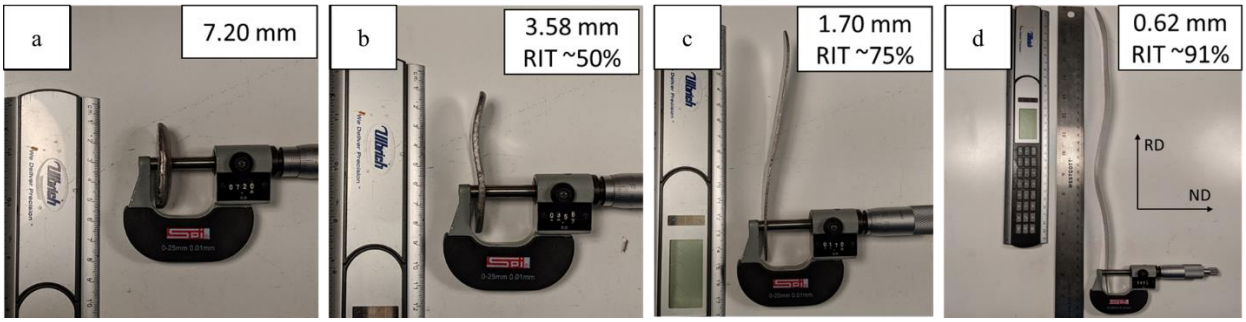

Fig. S1. Images for cold-rolled NTTHZ RHEA from the as-cast state to a RIT over 90%, showing excellent cold-workability. (A) As-cast state; (B) RIT=50%; (C) RIT=75%; (D) RIT=91%. RD – rolling direction, ND – normal direction.

Fig. S2. Images for cold rolled Nb-25Ta-15Ti-based RHEAs from the as-cast state to a reduction in thickness (RIT) over 90%, showing high processability at room temperature. (a) Nb-25Ta-15Ti matrix; (b) Nb-25Ta-15Ti-10Hf RHEA; (c) Nb-25Ta-15Ti-15Hf RHEA.

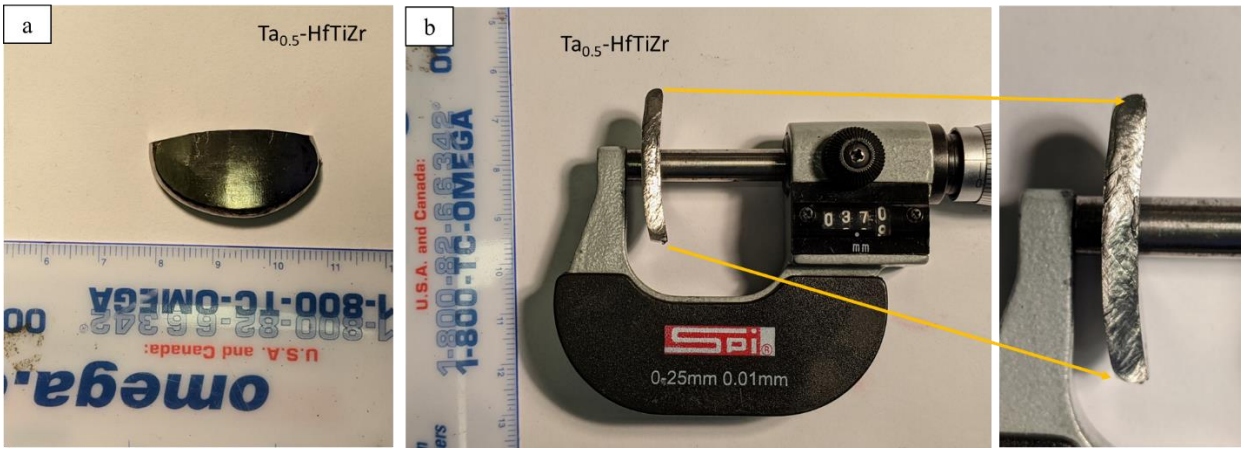

Fig. S3. Images for cold-rolled Ta0.5-HfTiZr RHEA with RIT less than 40%. (a) Several cracks appear in the surface; (b) Cracks penetrate through the whole sample, showing limited cold-workability of this alloy at room temperature.

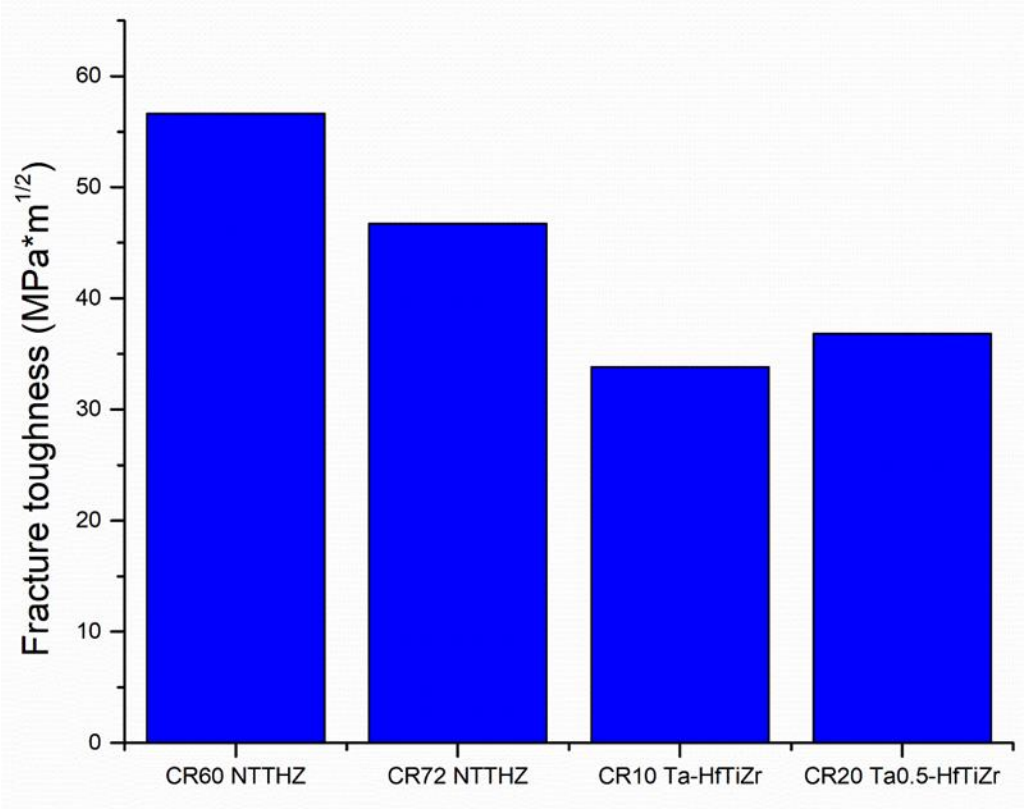

Fig. S4. Comparison of fracture toughness of cold-rolled $Hf_{15}Nb_{40}Ta_{25}Ti_{15}Zr_5$ (NTTHZ) with other ductile RHEAs at ambient temperature. CR60 – cold rolled to reduction in thickness of 60%.

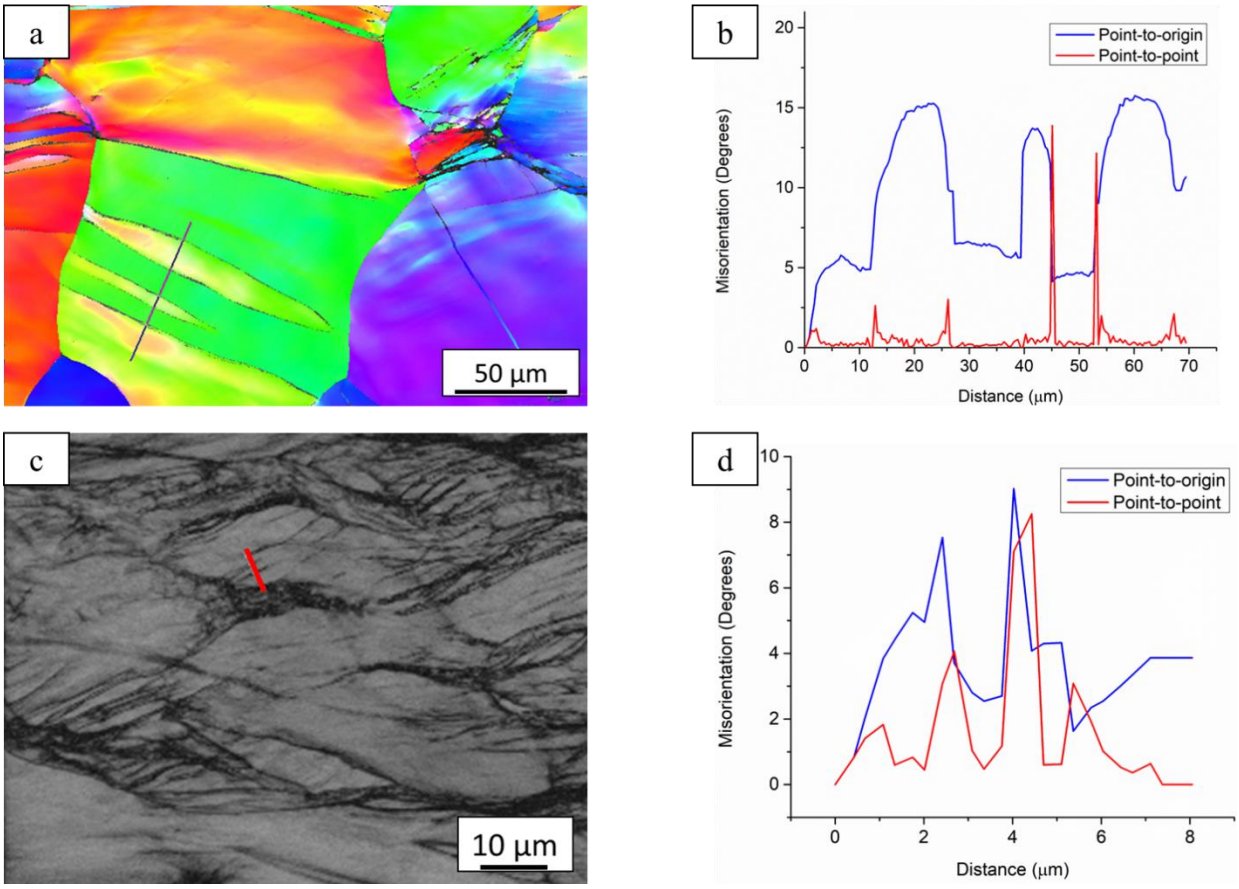

Fig. S5. EBSD micrographs and related misorientation profiles for cold-rolled $Hf_{15}Nb_{40}Ta_{25}Ti_{15}Zr_5$ RHEA with RIT of 30% and 60%. (a) EBSD IPF for $Hf_{15}Nb_{40}Ta_{25}Ti_{15}Zr_5$ with RIT of 30%, showing existence of microbands; (b) misorientation profiles for the labelled microbands in (A); (c) EBSD band contrast (BC) image for $Hf_{15}Nb_{40}Ta_{25}Ti_{15}Zr_5$ with RIT of 60%; (d) misorientation profiles for the labelled microbands in (c).

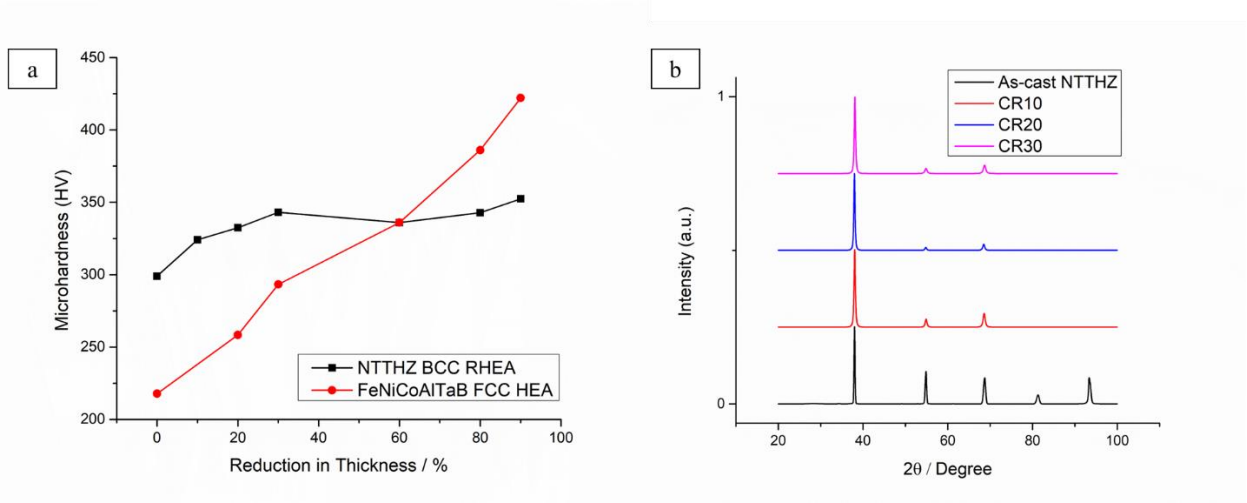

Fig. S6. Mechanical properties and phase evolution during the cold rolling process of $Hf_{15}Nb_{40}Ta_{25}Ti_{15}Zr_5$ RHEA. (A) Microhardness development of cold-rolled $Hf_{15}Nb_{40}Ta_{25}Ti_{15}Zr_5$(NTTHZ) RHEA and FCC Fe-27.5Ni-17.5Co-10.5Al-2.2Ta-0.04B HEA. (B) XRD patterns for cold-rolled $Hf_{15}Nb_{40}Ta_{25}Ti_{15}Zr_5$ (NTTHZ) RHEA from the as-cast state to RIT of 30%, showing single BCC phase.

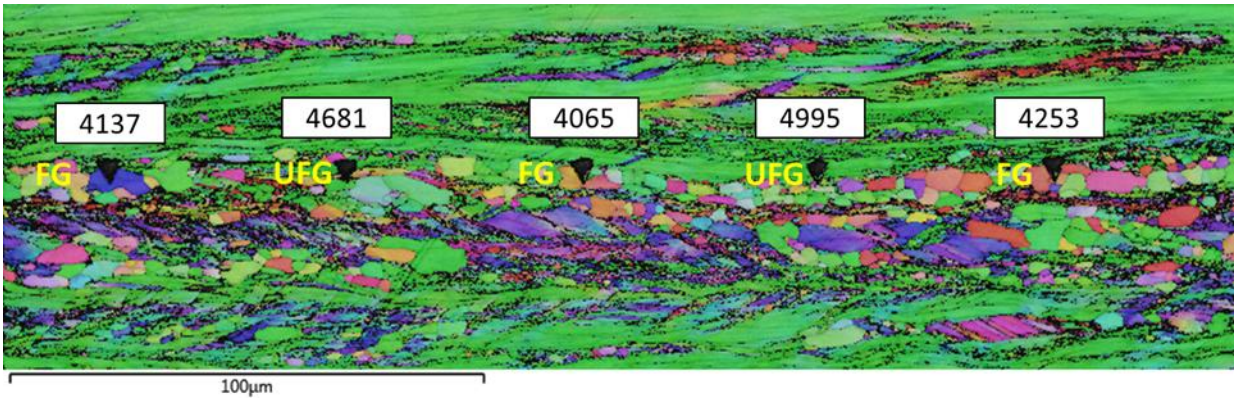

Fig. S7. EBSD inverse pole figure for the HL- NTTHZ RHEA after nanoindentation test. The number represents the value of microhardness of each point, unit: MPa. UFGs show much higher hardness than FGs.

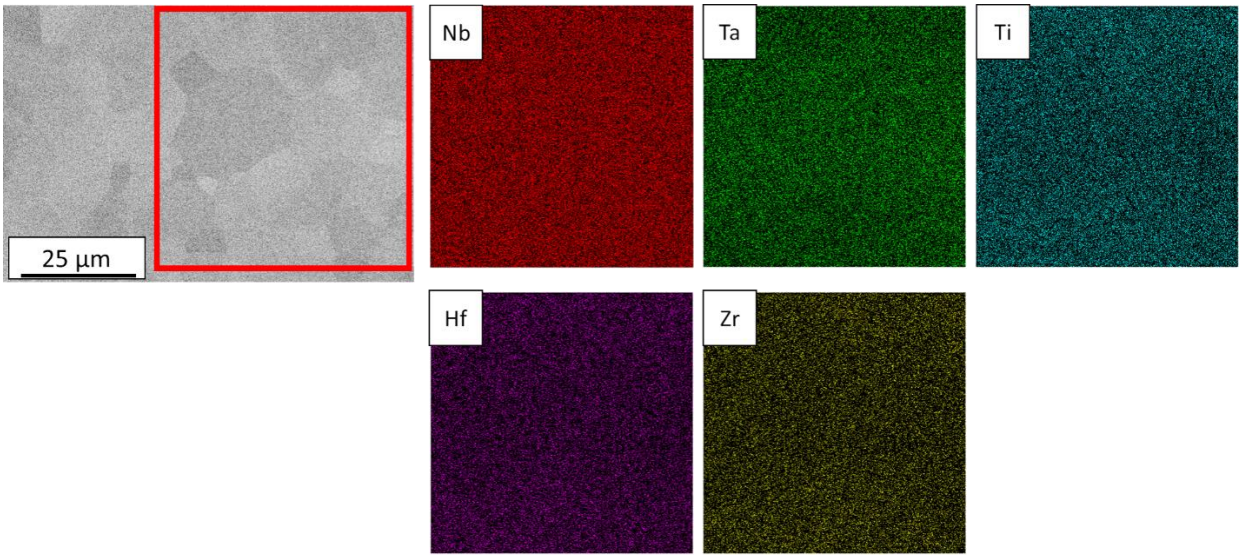

Fig. S8. SEM (BSE) micrograph and related EDS mapping results for CR90 $Hf_{15}Nb_{40}Ta_{25}Ti_{15}Zr_5$ RHEA after annealing at 1150ºC for 1 h, showing no element segregation.

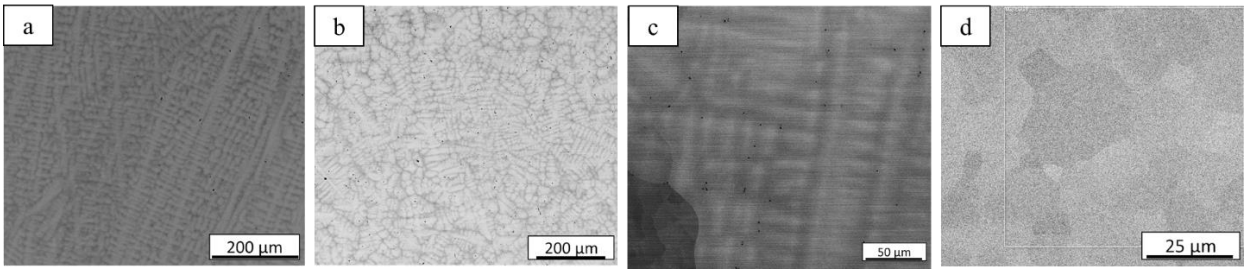

Fig. S9. SEM (BSE) micrographs for as-cast or cold-rolled Nb-25Ta-15Ti-based RHEAs after annealing at different conditions. (a) As-cast Nb-25Ta-15Ti matrix, annealed at 1500^{o}C for 12 h, still showing a dendrite structure. (b) As-cast Nb-25Ta-15Ti-7Mo, annealed at 1500^{o}C for 12 h, showing a dendrite structure and element segregation. (c) As-cast $Hf_{15}Nb_{40}Ta_{25}Ti_{15}Zr_5$ RHEA, annealed at 1300^{o}C for 12h, dendrite structure still exists. (d) Cold-rolled $Hf_{15}Nb_{40}Ta_{25}Ti_{15}Zr_5$ RHEA with RIT of 90%, annealed 1150^{o}C for 1 h, fine equiaxed grains form, no element segregation observed.

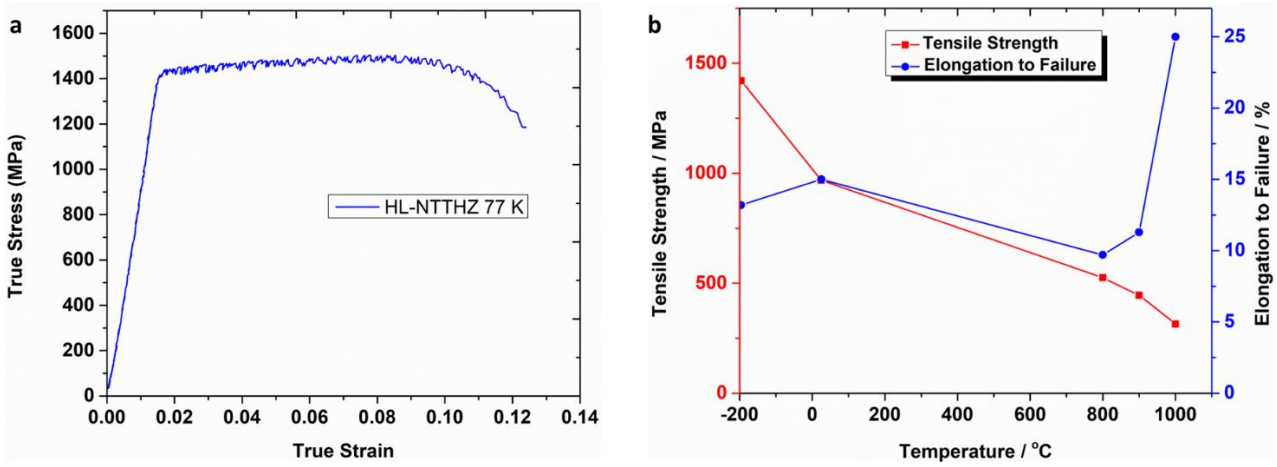

Fig. S10. (a) True tensile stress-strain curves of HL-NTTHZ RHEA tested at 77K (-196°C). (b) Development of strength and ductility of HL- NTTHZ RHEA tested at cryo-to-elevated temperatures.

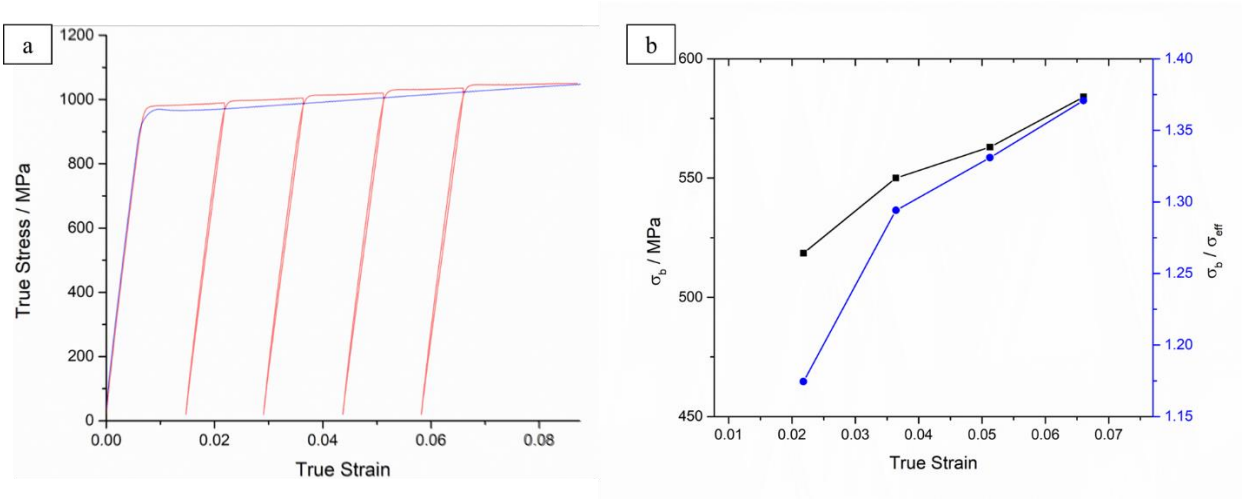

Fig. S11. Back-stress measurement of HL- NTTHZ RHEA at ambient temperature. (A) Loading-unloading-reloading cyclic tensile test for HL- NTTHZ RHEA at room temperature, showing obvious Bauschinger effect. (B) Comparison of back stress and effective stress during LUR cyclic tensile test.

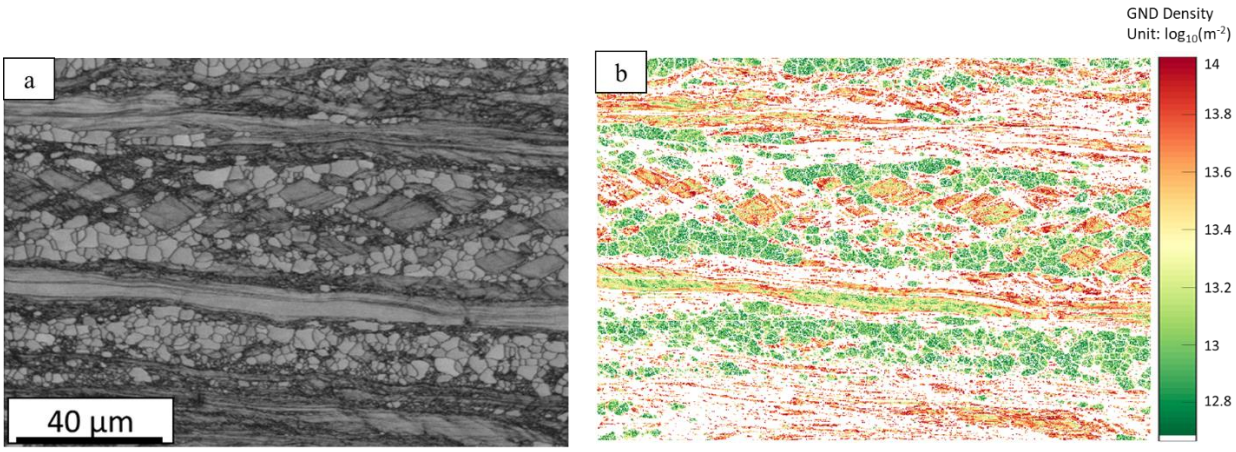

Fig. S12. Microstructure of HL- NTTHZ before tensile tests. (a) EBSD band contrast (BC) image for HL- $Hf_{15}Nb_{40}Ta_{25}Ti_{15}Zr_5$ RHEA before tensile test; (b) Corresponding GND density map to (a).

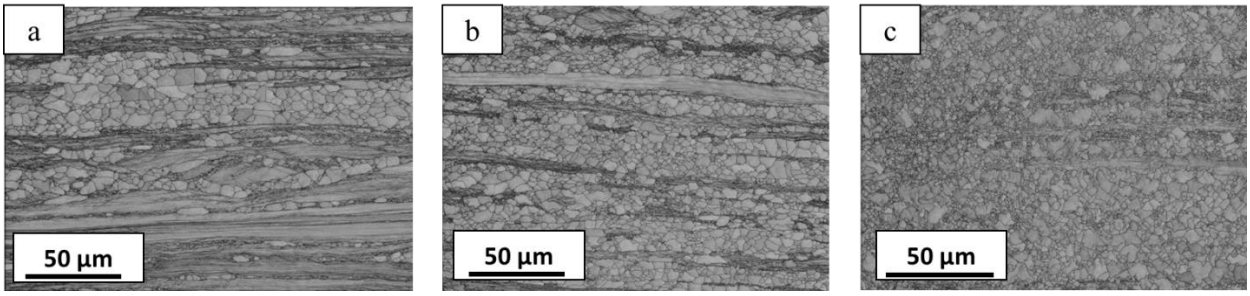

Fig. S13. Microstructure of HL- NTTHZ RHEA after testing at elevated temperatures. EBSD band contrast (BC) image for HL- $Hf_{15}Nb_{40}Ta_{25}Ti_{15}Zr_5$ RHEA after tensile tests at elevated temperatures. (a) 800°C; (b) 900°C; (c) 1000°C.

Supplementary Table 1

Supplementary Table 1. Dimensions of cold-rolled $Hf_{15}Nb_{40}Ta_{25}Ti_{15}Zr_5$ RHEA and other ductile RHEA for four-point bending tests (unit: mm)

	CR60	CR72	Ta-HfTiZr CR10	Ta(0.5)-HfTiZr CR20
W	2.80	3.20	3.70	3.20
B	1.41	1.58	1.88	1.6
L	4	4	4	4
a	1.36	1.56	1.79	1.55
a/W	0.486	0.488	0.484	0.484

Supplementary Table 2

Supplementary Table 2. Comparison of tensile properties between $Hf_{15}Nb_{40}Ta_{25}Ti_{15}Zr_5$ and HfNbTaTiZr RHEAs at different temperatures

Materials	Testing Temperature (K)	Tensile strength (MPa)	Elongation (%)	Grain Size (μm)	Comments
$Hf_{15}Nb_{40}Ta_{25}Ti_{15}Zr_5$	77	1503	13.4	0.7; 4.4	This work
	298	1068	14.8	0.7; 4.4	This work
	298	915	15.5	9.9	This work
	298	870	17.6	22.8	This work
	1073	550	10.8	0.7; 4.4	This work
	1273	325	24.8	0.7; 4.4	This work
HfNbTaTiZr	77	1630	11	60	Ref. 30
	77	1700	20	80	Ref. 67
	298	1260	9.7	22	Ref. 24
	298	1150	13.9	24.4	Ref. 25
	298	1185	18	31.3	Ref. 25
	298	1160	12.2	38.4	Ref. 25
	298	1090	15.5	40	Ref. 26
	298	1050	12.6	87	Ref. 26
	298	1020	10.4	112	Ref. 26
	298	890	9.2	100	Ref. 27
	298	1900	7.9	0.05	Ref. 27
	298	1100	20	38	Ref. 28
	298	1060	17	38	Ref. 28
	298	1030	15	128	Ref. 28
	298	1070	21	60	Ref. 30
	298	990	21	80	Ref. 67

****

2. In page 3, materials preparation. The authors provide "All Nb-25Ta-15Ti-based RHEA ingots were produced by arc-melting a mixture of high purity raw materials (Nb, Ta, Ti, Hf, Zr, Mo, W, all over 99.9 wt.% purity) under an Ar atmosphere". But the W and Mo elements are not used in the subsequent discussion of the article, which needs to be explained by the authors.

We thank the reviewer for this question. In the original manuscript, we added Mo and W to the materials preparation part by accident. We already removed “Mo and W” from the materials preparation part (Page 3). Thanks for reviewer’s kind reminder.

****

3. In page 8, The authors provide "Based on the misorientation profiles in Fig. 1(e-h), the deformation-induced twins with 60° misorientation are from the {112}<111> twin system, while those with approximately 50° misorientation are associated with the {332}<113> twin system". Such misorientation is due to the dislocation pile-up produced during heavy cold rolling, rather than twin structures. In addition, the authors did not observe the twin structure in the subsequent TEM characterization. The authors should make a more accurate analysis of this structure.

We thank the reviewer for these comments. Utilizing EBSD-based misorientation method to determine twins and deformation-induced bands is a widely accepted technique and has been demonstrated in previous work of β-Ti alloys and gum metals ([1][2][3]) . For example, as shown in Fig. R2 ([1]), the coincidence side site lattice (CSL) of the {112}<111> twin is determined to be a Σ3 boundary, which corresponds to a misorientation of 60° around <111> (Fig. R2b). For the twinning system {332}<113> the CSL boundary is Σ11, which corresponds to a misorientation of 50.5° around <110> (Fig. R2c). Therefore, our statement about deformation-induced twins in the manuscript is reasonable in line with established procedures in the literature. In addition, for deformation bands produced by dislocations, the misorientation is usually less than 30°, as shown in the original Fig. S5 (currently in Fig. R3). These bands are usually termed as kink bands or microbands ([2][4][5]). Kinking is a type of cooperative deformation mechanism controlled by slip ([6]), and the formation of kink bands can improve the deformability of the crystal by stress relaxation and crystal reorientation ([2][4][7]). When the RIT reaches 80%, some shear bands appear (with an angle of 40-45° to the rolling direction), as shown in Fig. R4. For the subsequent TEM characterization, the reduction in thickness of is over 90%, which refers to severely plastic deformation. A high density of dislocations formed in the heavily-deformed sample, even the previously deformation-induced twins would transfer to some dislocation structure, like kind bands, shear bands, or lamellar bands, as shown in Fig. R3, R4, and Fig. 1i.

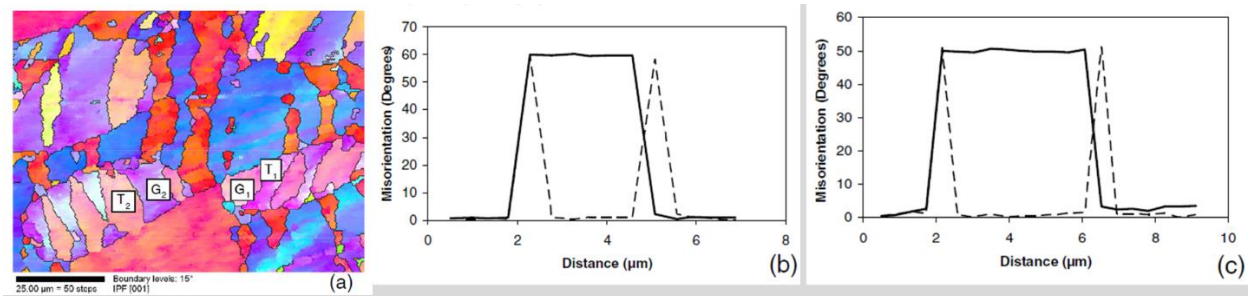

Fig. R2 Inverse pole figure of β-Ti (Ti-25Ta-24Nb) alloy (a) after tensile testing and (b) misorientation profiles between G1 and T1 and (c) between G2 and T2. Solid line, point to origin; dotted line, point to point ([1]).

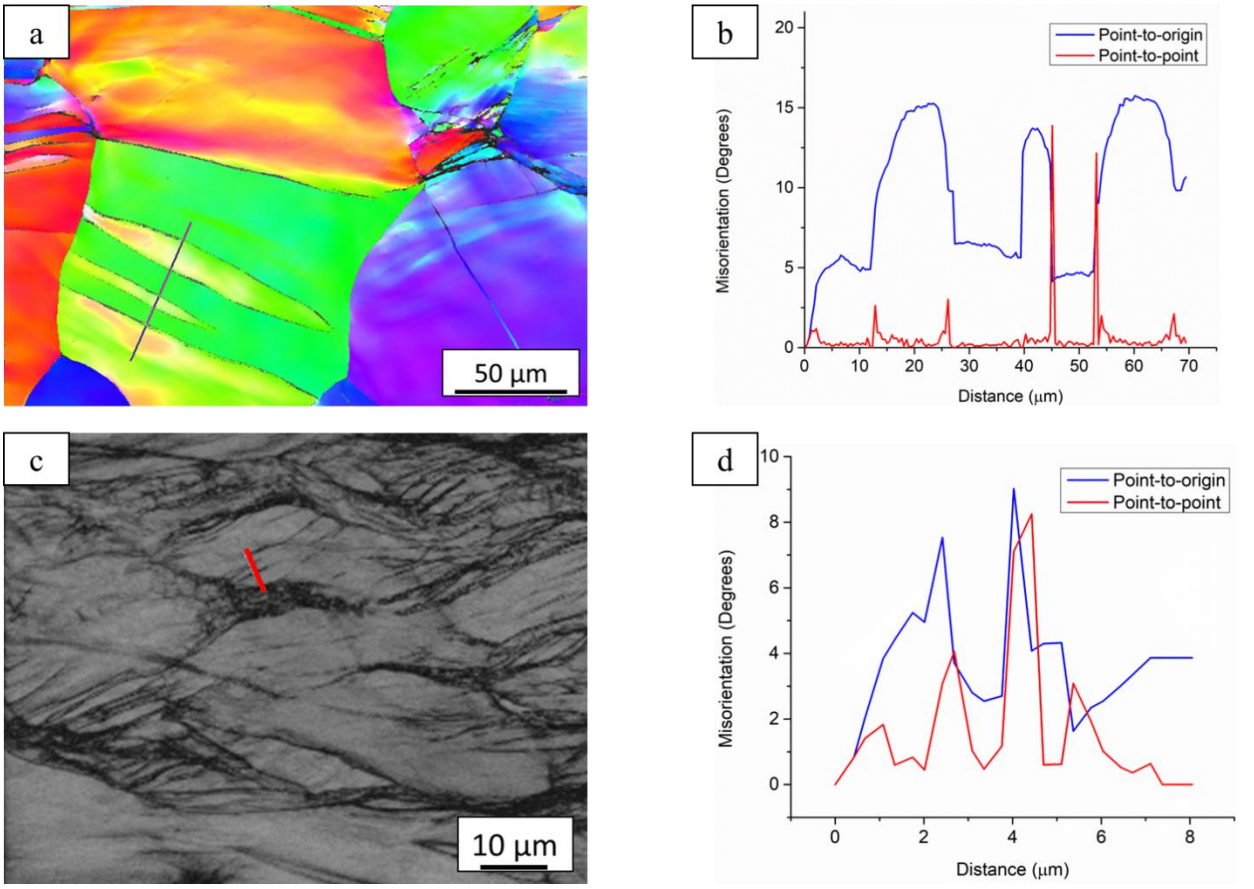

Fig. R3. EBSD micrographs and related misorientation profiles for cold-rolled Hf15Nb40Ta25Ti15Zr5 RHEA with RIT of 30% and 60%. (a) EBSD IPF for Hf15Nb40Ta25Ti15Zr5 with RIT of 30%, showing existence of microbands; (b) misorientation profiles for the labelled microbands in (A); (c) EBSD band contrast (BC) image for Hf15Nb40Ta25Ti15Zr5 with RIT of 60%; (d) misorientation profiles for the labelled microbands in (c).

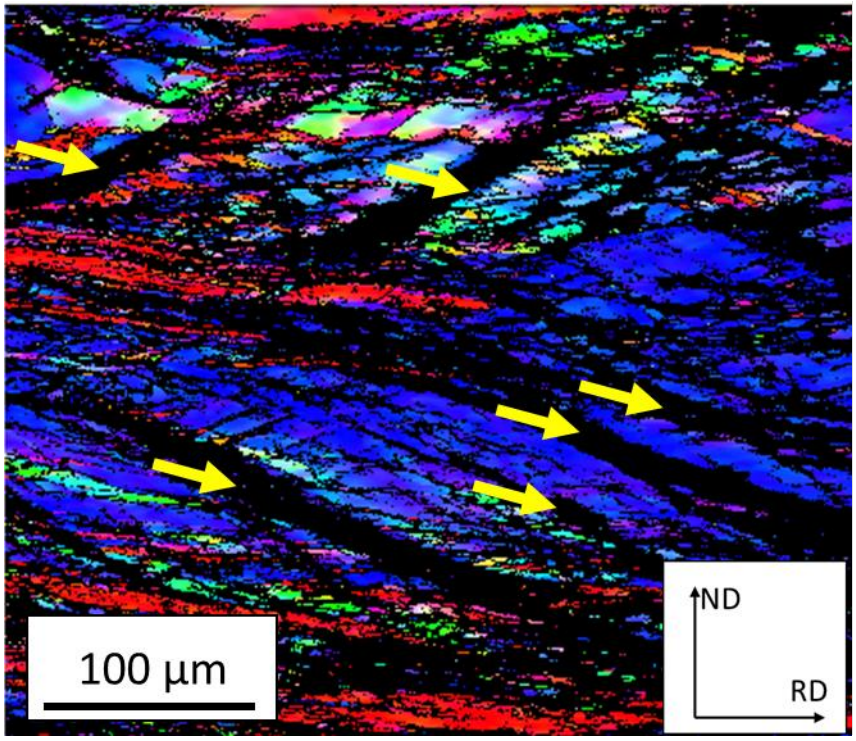

Fig. R4 EBSD micrograph of cold-rolled NTTHZ specimen with RIT=80%. Yellow arrows show the formation of shear bands. ND - normal direction; RD - rolling direction.

****

4. In page 10, Deformation mechanism during cold rolling. The authors provide "Nb60Ta25Ti15 yields by deformation twinning, involving a reorientation of the crystal lattice within twinned volumes of the materials". Atomic simulation of uniaxial compression of Nb60Ta25Ti15 is difficult to explain the deformation mechanism of Hf15Nb40Ta25Ti15Zr5. These two materials are very different in composition, and the deformation mechanism may also be disparate. For example, the alloying element content will have a great influence on the stacking fault energy. In addition, no twin structure was observed by TEM analysis. The author should rediscuss this part.

We thank the reviewer for these comments. It is noted that Nb60Ta25Ti15 is our base alloy composition and that it shows exceptional formability. The aim of the atomistic simulation is to reveal the role of concentrated solid solutions (mixing of Nb, Ta, and Ti, the three base elements in our alloys) on deformation mechanisms by comparing them to pure Nb. As illustrated in Figure 8, the addition of Ta and Ti (i.e., Nb60Ta25Ti15) promotes twinning deformation. It is reasonable to speculate that further addition of Hf and Zr would influence twinning as its effect on stacking faulty energy modulation, as pointed out by the reviewer. The relationship between composition, stacking faculty energy, and twinning propensity deserve further and careful study.

In the revised manuscript, on Page 11, we have added the following text:

"It is noted that Nb60Ta25Ti15 is our base alloy composition and that it shows exceptional formability. The aim of the atomistic simulation is to reveal the role of concentrated solid solutions (mixing of Nb, Ta, and Ti, the three base elements in our alloys) on deformation mechanisms by comparing them to pure Nb. As illustrated in Figure 8, the addition of Ta and Ti (i.e., Nb60Ta25Ti15) promotes twinning deformation. It is reasonable to speculate that further addition of Hf and Zr would influence twinning as its effect on stacking faulty energy modulation. The relationship between composition, stacking faculty energy, and twinning propensity deserve further and careful study."

In addition, the previous EBSD results in Fig. 1(e-h) already shows the appearance of deformation-induced twins. As we mentioned in the answer to Question 4, the misorientation profiles from EBSD results are a convincible method to prove the existence of deformation-induced twins.

****

5. In page 11, Comparison of mechanical property at elevated temperatures. The authors provide "In the case of CMSX-4 and CMSX-10, a high content of Ta and W are added to strengthen the matrix and increase the volume fraction of γ'". The addition of Ta element to the nickel-based superalloys will induce γ'' precipitate with D022 structure instead of γ' precipitate with L12 structure. In addition, W element is added to improve the thermal stability of the alloy.

We thank the reviewer for these comments. In the Ni-based superalloys, the addition of Ta can help to induce γ' precipitates with L12 structure, while the addition of Nb will induce γ'' precipitates with D022 structure ([8] R.C. Reed, The superalloys: fundamentals and applications, Cambridge university press, 2008.). Therefore, the statement in the original manuscript is reasonable. It is correct that "W element is added to improve the thermal stability of the alloy". Therefore, we added "W element is added to improve the thermal stability of the alloy" to the revised manuscript (Page 11).

****

6. In page 12, Deformation mechanism in heterogeneous-structured RHEAs. The authors provide "The TEM micrograph in Fig. 10c shows that UFG domains have higher dislocation densities compared to FG regions when the plastic strain reaches 0.08". There are few FG regions in TEM image (Fig. 10c), so it is difficult to determine the distribution of dislocation density in FG regions. In the UFG regions, the dislocation distribution is relatively uniform, although there is a certain pileup at the grain boundaries, but this is a normal phenomenon in the deformation process. Hence, it is difficult to prove the back stress hardening effect. Moreover, Figure 10c should be STEM-HAADF image rather than DF.

We thank the reviewer for these comments. Yes, the original Fig. 10c is a STEM-HAADF image. We tried to take STEM-HAADF micrographs for the fine-grained areas and ultrafine-grained regions. However, the orientation of ultrafine grains is random, which leads to the arbitrary distribution of dislocation density when the specimen is tilted to some angle. In order to prove the back stress hardening effect, following Wu's EBSD-based method ([9]), we first obtained statistics of true strain in each fine grain when the global true strain is ~0.08. The true strain in each grain can be calculated from its aspect ratio α as $\varepsilon = (2/3)\ln\alpha$, where $\alpha = w/l$, and w, l is the width and length of the fine grain, respectively. The average true strain in elongated fine grains is 0.36 when the hetero-structured specimen is deformed to a global true strain of ~0.08 (see Fig. R5b). Meanwhile, most ultrafine grains remain equiaxed at the strain of 0.08 (see Fig. R5c). This difference in plastic strain between fine grains (strain =0.36 > 0.08) and ultrafine grains (strain <0.08) gives rise to plastic strain partitioning. The strain has to be continuous at the FG/UFG interfaces, which further leads to strain gradient near these interfaces. Accommodation of such strain gradient requires the generation of geometrically necessary dislocations (GNDs) ([10][11]). As a consequence, long-range back stresses are created and essentially work as a strain hardening mechanism.

In the revised manuscript, on Page 13, we have added the following text:

"The EBSD IPF image in Fig. 10c shows that most of the fine grains are elongated when the HL specimen is applied with a global strain of 0.08. The true strain in each grain can be calculated from its aspect ratio α as $\varepsilon=(2/3)\ln\alpha$, where $\alpha=w/l$, w and l is the width and length of the fine grain, respectively [36]. The average true strain in fine grains is calculated as 0.36, as shown in Fig.10d. Meanwhile, most ultrafine grains remain equiaxed at the strain of 0.08 (see Fig. 10e). This difference in plastic strain between fine grains (strain = 0.36 > 0.08) and ultrafine grains (strain < 0.08) gives rise to plastic strain partitioning. The plastic deformation has to be continuous at the FG/UFG interfaces, which further causes strain gradient near these interfaces. Accommodation of such strain gradient requires the generation of geometrically necessary dislocations (GNDs) [69][70]. As a consequence, long-range back stresses are created and essentially work as a strain hardening mechanism".

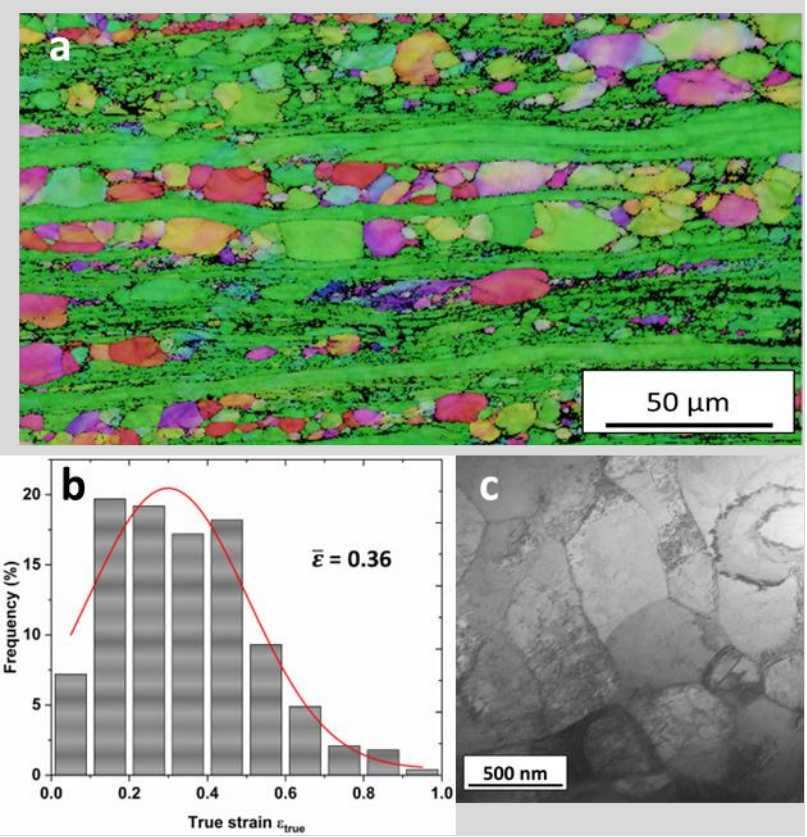

Fig. R5 Strain partitioning in the HL-NTTHZ specimen with an applied strain of 0.08. (a) EBSD IPF image showing most fine grains are elongated along tensile direction at the strain of 0.08; (b) Distribution of strains in fine grains with an average true of 0.36; (c) TEM micrograph showing equiaxed ultrafine grains in the HL specimen with a strain of 0.08.

References

[1] E. Bertrand, P. Castany, I. Péron, T. Gloriant, Twinning system selection in a metastable β-titanium alloy by Schmid factor analysis, Scr. Mater. 64 (2011) 1110–1113.

[2] Y. Yang, S.Q. Wu, G.P. Li, Y.L. Li, Y.F. Lu, K. Yang, P. Ge, Evolution of deformation mechanisms of Ti–22.4 Nb–0.73 Ta–2Zr–1.34 O alloy during straining, Acta Mater. 58 (2010) 2778–2787.

[3] S. Shin, C. Zhang, K.S. Vecchio, Phase stability dependence of deformation mode correlated mechanical properties and elastic properties in Ti-Nb gum metal, Mater. Sci. Eng. A. 702 (2017) 173–183.

[4] S. Zherebtsov, N. Yurchenko, D. Shaysultanov, M. Tikhonovsky, G. Salishchev, N. Stepanov, Microstructure and Mechanical Properties Evolution in HfNbTaTiZr Refractory High-Entropy Alloy During Cold Rolling, Adv. Eng. Mater. 22 (2020) 2000105.

[5] S. Sadeghpour, S.M. Abbasi, M. Morakabati, L.P. Karjalainen, Effect of

dislocation channeling and kink band formation on enhanced tensile properties of a new beta Ti alloy, J. Alloys Compd. 808 (2019) 151741.

[6] A.G. Crocker, J.S. Abell, The crystallography of deformation kinking, Philos. Mag. 33 (1976) 305–310.

[7] A.T. Churchman, The yield phenomena, kink bands and geometric softening in titanium crystals, Acta Metall. 3 (1955) 22–29.

[8] R.C. Reed, The superalloys: fundamentals and applications, Cambridge university press, 2008.

[9] X. Wu, M. Yang, F. Yuan, G. Wu, Y. Wei, X. Huang, Y. Zhu, Heterogeneous lamella structure unites ultrafine-grain strength with coarse-grain ductility, Proc. Natl. Acad. Sci. 112 (2015) 14501–14505.

[10] M.F. Ashby, The deformation of plastically non-homogeneous materials, Philos. Mag. 21 (1970) 399–424.

[11] H. Gao, Y. Huang, Geometrically necessary dislocation and size-dependent plasticity, Scr. Mater. 48 (2003) 113–118.

Reviewer #2: This manuscript reports a class of super-formable refractory high-entropy alloys, whose excellent cold workability is ascribed to the activation of a high-density of dislocations and deformation twins as well as the high diffusivity paths. It is well structured and written. In my opinion, it is of great interest for the readers of Acta Materialia. My comments are as follows.

We thank the reviewer for the positive comments.

****

Page 4
Was the strain rate kept constant during tensile testing? Or the given value on this page is just the initial strain rate? How was the strain measured?

We thank the reviewer for the question. Yes, during the tensile tests at -196°C and room temperature, an extensometer was used to measure the strain accurately. During the tensile tests at elevated temperatures, the strain measurement was conducted using a non-contacting digital image correlation video extensometer (as shown in Fig. R1), where a speckle pattern is applied to the surface of the specimens with high temperature paint for tracking purposes. The video data were recorded at 10 frames per second and analyzed using the iMetrum Video Gauge software (S. Sulzer, et al., Metall. Mater. Trans. A. 49 (2018) 4214–4235). The strain rate was set as 1.0×10^{-3} s^{-1} in all tensile tests.

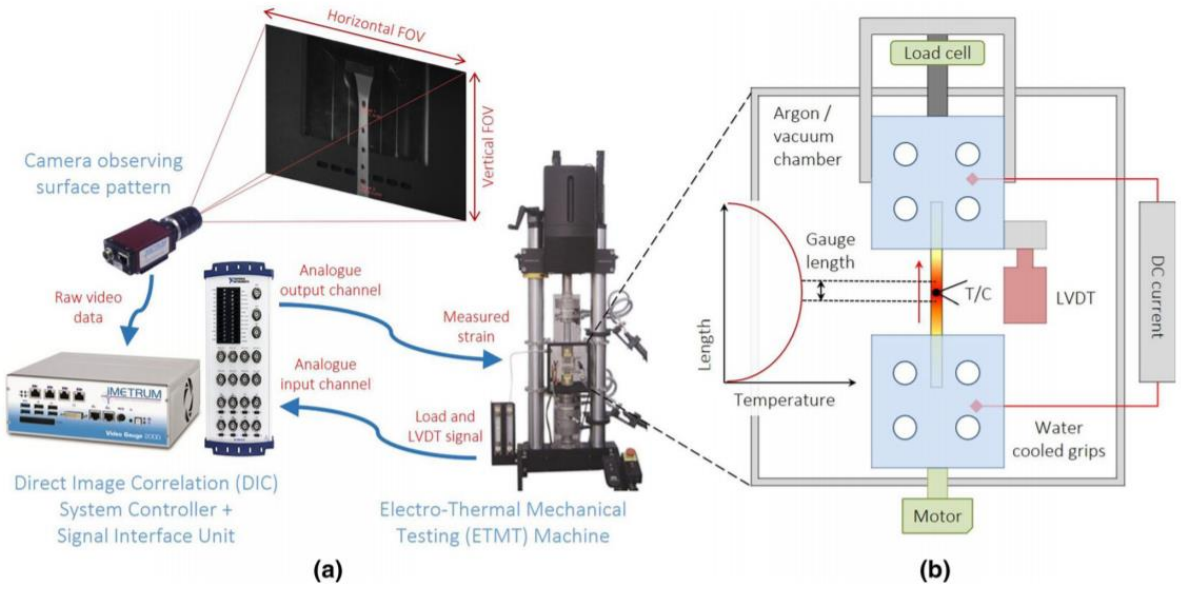

Fig. R1 (a) Overview of the testing system used for high-temperature testing of superalloys at Oxford University; (b) Schematic illustration of ETMT components. (S. Sulzer, et al., Metall. Mater. Trans. A. 49 (2018) 4214–4235.).

****

Page 8
Why is the formation of {332}<113> twins responsible for softening? Indeed, this type of twin has been revealed to significantly enhance the work hardening rate of metastable β Ti alloys (e.g., Scripta Mater. 69 (2013) 393-396 & Acta Mater. 151 (2018) 67-77).

We thank reviewer for this excellent question. Yes, this type of twin has been shown to enhance the work hardening rate of metastable β-Ti alloys effectively. We checked the reference cited in our original manuscript (S. Shin, et al., Mater. Sci. Eng. A. 724 (2018) 189–198), it is found that the softening phenomenon is mainly caused by cyclic annealing, instead of the deformation-induced twins. In the current study, apart from the formation of deformation-induced twins, some kink bands or microbands are also formed with misorientation less than 30°, as shown in Fig. S5. With RIT increasing from 30% to 60%, more and more kink bands are formed. When the RIT reaches 60%, most of deformation bands are kink bands, instead of twins. Kinking is a type of cooperative deformation mechanism controlled by slip (A.G. Crocker, et al., Philos. Mag. 33 (1976) 305–310.), and the increase in dislocation density at the initial deformation stage would activate kinking. The formation of kink bands can improve the deformability of the crystal by stress relaxation and crystal reorientation, leading to softening, which is also observed in β-Ti alloys, pure Ti, and Senkov alloy (1. Y. Yang, et al., Acta Mater. 58 (2010) 2778–2787. 2. S. Zherebtsov, et al., Adv. Eng. Mater. 22 (2020) 2000105. 3. A.T. Churchman, Acta Metall. 3 (1955) 22–29.). Therefore, we think the softening is caused by the formation of kink bands or microbands, instead of twins.

In the revised manuscript, on Page 8, we have added the following text:

“With RIT increasing from 30% to 60%, more and more deformation-induced kink bands are formed, while fewer twins are observed. These kink bands contribute to softening and formability of specimens via stress relaxation and crystal reorientation, which is also observed in β-Ti alloys, pure Ti, and the Senkov alloy”.

****

Page 12
Are the dislocations all visualized in Fig. 10c under only one diffraction condition? Is it possible that some dislocations are not shown due to inappropriate diffraction conditions? If so, the comparison in dislocation density is questionable.

We thank the reviewer for these comments. Yes, the dislocations are all visualized under one diffraction condition in the original manuscript. We tried to take dislocation distribution micrographs for the fine-grained areas and ultrafine-grained regions under two-beam conditions. However, the orientation of ultrafine grains is random, which leads to the

arbitrary distribution of dislocation density. In order to prove the back stress hardening effect, following Wu's EBSD-based method (X. Wu, et al., Proc. Natl. Acad. Sci. 112 (2015) 14501–14505.), we first made a statistic of true strain in each fine grain when the global true strain is ~0.08. The true strain in each grain can be calculated from its aspect ratio α as $\varepsilon = (2/3)\ln\alpha$, where $\alpha = w/l$, w, l is the width and length of the fine grain, respectively. The average true strain in elongated fine grains is 0.36 when the hetero-structured specimen is deformed to a global true strain of ~0.08 (see Fig. R2b). Meanwhile, most ultrafine grains remain equiaxed at the strain of 0.08 (see Fig. R2c). This difference in plastic strain between fine grains (0.36 > 0.08) and ultrafine grains (<0.08) gives rise to plastic strain partitioning. The strain has to be continuous at the FG/UFG interfaces, which further leads to strain gradient near these interfaces. Accommodation of such strain gradient requires the generation of geometrically necessary dislocations (GNDs) (1. M.F. Ashby, Philos. Mag. 21 (1970) 399–424. 2. H. Gao, Y. Huang, Scr. Mater. 48 (2003) 113–118.). As a consequence, long-range back stresses are created and essentially work as a strain hardening mechanism.

In the revised manuscript, on Page 13, we have added the following text:

"The EBSD IPF image in Fig. 10c shows that most of fine grains are elongated when the HL specimen is applied with a global strain of 0.08. The true strain in each grain can be calculated from its aspect ratio α as $\varepsilon=(2/3)\ln\alpha$, where $\alpha=w/l$, w and l is the width and length of the fine grain, respectively [36]. The average true strain in fine grains is calculated as 0.36, as shown in Fig.10d. Meanwhile, most ultrafine grains remain equiaxed at the strain of 0.08 (see Fig. 10e). This difference in plastic strain between fine grains (strain = 0.36 > 0.08) and ultrafine grains (strain < 0.08) gives rise to plastic strain partitioning. The plastic deformation has to be continuous at the FG/UFG interfaces, which further causes strain gradient near these interfaces. Accommodation of such strain gradient requires the generation of geometrically necessary dislocations (GNDs) [69][70]. As a consequence, long-range back stresses are created and essentially work as a strain hardening mechanism".

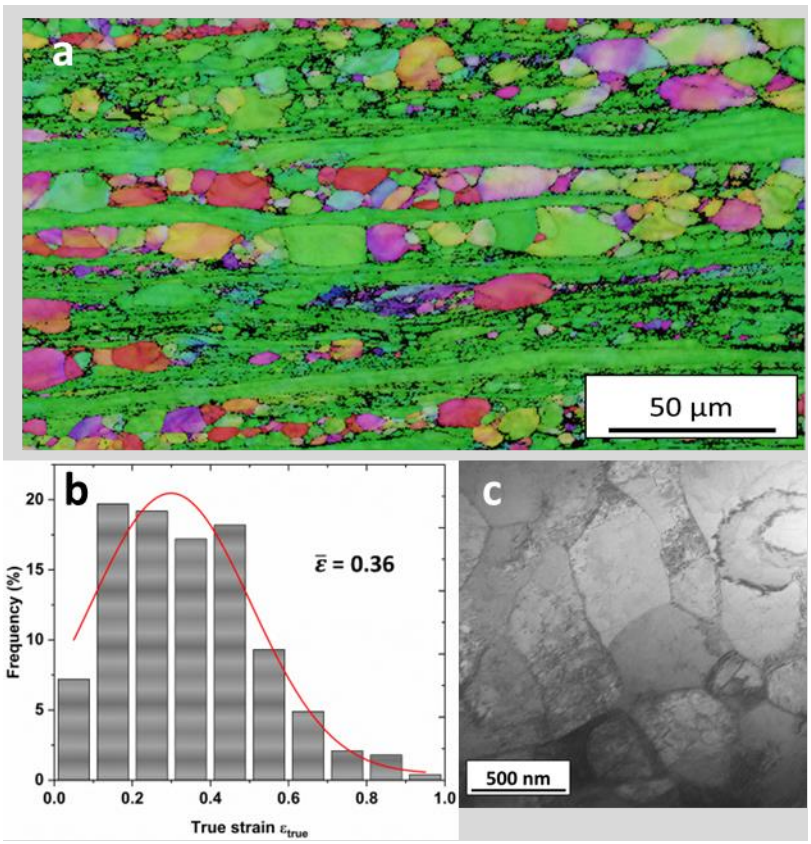

Fig. R2 Strain partitioning in the HL-NTTHZ specimen with an applied strain of 0.08. (a) EBSD IPF image showing most fine grains are elongated along tensile direction at the strain of 0.08; (b) Distribution of strains in fine grains with an average true of 0.36; (c) TEM micrograph showing equiaxed ultrafine grains in the HL specimen with a strain of 0.08.

Strong and Ductile Refractory High-Entropy Alloys with Super Formability

Authors: Cheng Zhang[1], Haoren Wang[2], Xinyi Wang[3], Yuanbo T. Tang[4], Qin Yu[5,6], Chaoyi Zhu[6], Mingjie Xu[1], Shiteng Zhao[6], Rui Kou[7], Xin Wang[1], Benjamin E. MacDonald[1], Roger C. Reed[4], Kenneth S. Vecchio[2], Penghui Cao[3], Timothy J. Rupert[1], Enrique J. Lavernia[1,*]

Affiliations:

[1] Department of Materials Science and Engineering, University of California Irvine, Irvine, CA 92697, USA

[2] Department of NanoEngineering, University of California San Diego, La Jolla, CA 92093, USA

[3] Department of Mechanical and Aerospace Engineering, University of California Irvine, Irvine, CA 92697, USA

[4] Department of Materials, University of Oxford, Parks Road, Oxford, OX1 3PH, United Kingdom

[5] Materials Sciences Division, Lawrence Berkeley National Laboratory, Berkeley, CA 94720, USA

[6] Department of Materials Science and Engineering, University of California, Berkeley, CA 94720, USA

[7] Department of Structural Engineering, UC San Diego, La Jolla, CA 92093, USA

*Corresponding author. Email: lavernia@uci.edu

Abstract: Refractory high-entropy alloys (RHEAs) are considered promising candidate materials for high-temperature structural applications that currently use superalloys. However, for most of the reported RHEAs, their poor ductility and negligible cold-workability at room temperature have hindered their use. Here, we report a new class of non-equiatomic NbTaTi-based RHEAs that can be cold-rolled to a reduction of over 90% from the as-cast state without surface treatment and/or intermediate annealing. This excellent cold-workability is facilitated by activation of a high-density of dislocations and deformation twins as well as by high diffusivity paths, such that these RHEAs can be rendered homogeneous at lower annealing temperatures for much shorter time durations. In addition, we report that the RHEAs retain their high strength at elevated temperatures and exhibit considerable ductility at cryogenic conditions, evading the traditional strength–ductility trade-off. This class of super-formable RHEAs provides a novel design pathway to fabricate high-temperature structural materials via an energy- and time-saving method.

Keywords: Refractory high-entropy alloys; formability; cryogenic-to-elevated temperatures; strength-ductility synergy;

1. Introduction

As a new class of metallic materials, high-entropy alloys (HEAs) or complex concentrated alloys composed of four or more principal elements significantly expand the space of alloy design [1][2][3]. An increasing number of attractive properties have been discovered in HEAs over a wide temperature range, including excellent strength-ductility synergy at ambient temperature [4][5][6] , exceptional mechanical properties at cryogenic temperatures [7], and ultrahigh strength at elevated temperatures [8]. Among various kinds of HEAs, refractory HEAs (RHEAs) stand out due to their unparalleled mechanical properties at high temperatures over 800^{o}C and even up to 1500^{o}C in some cases [9][10][11], which enables them to be promising candidates for high-temperature structural applications, outperforming conventional Ni-based superalloys. To date, a significant effort from the metallurgy community has focused on developing RHEAs with high processibility and outstanding strength-ductility synergy at ambient temperature. However, for most RHEAs, their ultra-high strength comes with very limited ductility [12][13]; as a result, tensile ductility is rarely reported for these alloys as it is commonly negligible. Furthermore, the poor cold-workability at room temperature makes the elimination of the as-cast microstructure difficult through conventional rolling and heat treatment processes, which greatly limits the application of RHEAs. For most of the reported RHEAs with reasonable ductility at room temperature, the mechanical properties were measured in their as-cast state [14][15][16], which is susceptible to stochastic premature failure due to casting defects including porosity, dendritic grain structure, and appreciable elemental segregation formed during the solidification process. For conventionally processed RHEAs, extended high-temperature homogenization (24 – 168 h at over 0.7T_m, where T_m is the melting point) is needed for the as-cast samples to achieve a uniform microstructure due to extremely low diffusion rates for the alloy constituents [8], a processing routine which is both time and energy intensive. Therefore, the design and fabrication of RHEAs with high processibility and good tensile strength-ductility synergy at room temperature remains a paramount challenge. Inspired by the HfNbTaTiZr (Senkov alloy) RHEA and some RHEAs derived from the original Senkov alloy, some criteria were put forward and subsequently revised to improve the ductility of RHEAs at room temperature [17][18][19][20][21][22][23]. The Senkov alloy processed

through homogenization or surface treatment can indeed show good cold workability and tensile ductility at ambient temperature [24][25][26][27][28][29][30][31][32][33]. However, the surface treatment to remove casting defects, as reported in these studies, would result in a considerable material waste and cost increases [26][31][32].

In addition to designing new alloy compositions, the tailoring of internal microstructures provides an another effective approach to surmount the traditional strength-ductility tradeoff in metals and alloys, especially by the introduction of a heterogeneous microstructure [34][35]. For example, heterogeneous lamella (HL) structures [36], bimodal structures [37][38], and gradient structures [39][40] have been engineered with targeted microstructural heterogeneities to achieve high strength, while maintaining ductility in metallic materials. Engineering of microstructural heterogeneities can be implemented to promote delocalization of strain and enhancement of work hardening ability, which helps to prevent the early formation of necking during the plastic deformation[34]. Recently, HEAs with heterogenous microstructures have successfully achieved high strength-ductility synergy [41][42][43]. However, it is important to note that these studies only focus on face centered cubic (FCC) HEAs, which already generally have good processibility. The application of heterogeneous microstructures to body centered cubic (BCC) RHEAs has been rarely reported to date due to the significant difficulty in thermomechanical processing, which underscores the novelty of the present work.

2. Experimental Procedures

2.1 Materials Preparation

All Nb-25Ta-15Ti-based RHEA ingots were produced by arc-melting a mixture of high-purity raw materials (Nb, Ta, Ti, Hf, Zr, all over 99.9 wt.% purity) under an Ar atmosphere. In the arc-melter chamber, a high-purity Ti-getter was used to absorb residual oxygen before arc-melting raw materials. In order to promote homogeneity, each RHEA ingot was flipped and re-melted for 5-8 times. The weight of as-cast samples was between 30 and 70 grams. Some as-cast samples were processed through conventional homogenization at 1250 – 1500°C for 10 – 18 h for comparison with thermomechanical-processed

samples. Some as-cast samples with thickness of 6-7 mm were processed through thermomechanical processing, including cold rolling with a reduction in thickness (RIT) up to 91%, annealing (900 – 1300°C, 0.5-1 h) and water quenching.

2.2 Mechanical testing

Room-temperature tensile test samples with a gauge length of 18 mm and a cross-section of 3 x (0.5-0.7) (mm^2) were produced by electrical discharge machining (EDM). Before room-temperature tensile testing, samples were ground and polished to a mirror surface with SiC papers up to 4000 grit. “Loading-unloading-reloading” (LUR) cyclic tension tests were conducted to calculate the back-stress of samples with heterogeneous lamella (HL) structure. The strain rate in the current study is set to $1x10^{-3}$ s^{-1}. Microhardness of samples were measured by Vicker’s hardness testing (Leica Hardness Testing Machine). Load and loading time for microhardness test were 500 gf and 15 s, respectively. At least 10 data points were used for each measurement of the reported values. Besides, the hardness of fine grain (FG) and ultrafine grain (UFG) regions were evaluated using KLA (formerly KEYSIGHT) G200 Nanoindenter. Load, loading time and holding time for the test were 50 mN, 5 s and 2 s, respectively. Four-point bending test was employed to measure the fracture toughness of cold-rolled $Hf_{15}Nb_{40}Ta_{25}Ti_{15}Zr_5$ and other ductile RHEAs. The stress-intensity factor K in the four-point bending test can be calculated by Equation (1) [44],[45]:

$$K = \frac{3PL}{BW^2}\sqrt{\pi a}\left[1.122 - \frac{1.121a}{W} + 3.740\left(\frac{a}{W}\right)^2 + 3.873\left(\frac{a}{W}\right)^3 - 19.05\left(\frac{a}{W}\right)^4 + 22.55\left(\frac{a}{W}\right)^5\right] \quad (1)$$

where P is the load, B is the thickness, W is the width, a is the crack size, L = (S1-S2)/2, with S1 and S2, the external (16 mm) and internal (10 mm) spans. The samples were pre-cracked to a crack length/width ratio, a/W~ 0.5, consistent with ASTM E399. Related dimensions of samples for the four-point bending test are shown in Table S1.

For $Hf_{15}Nb_{40}Ta_{25}Ti_{15}Zr_5$ RHEA samples, high temperature tensile tests were conducted using an Instron Eletro-Thermal Mechanical Testing (ETMT) system [46]. The samples were first machined by electric-discharge machining (EDM) into plate specimens with a cross-sectional area of 2 x (0.5-0.7) mm^2, which is followed by grinding with abrasive media up to 4000 grit to a mirror finish. A K-type thermocouple was spot-welded at the

center of the specimen to monitor and control temperature during testing. Heating was achieved via the joule effect by direct current at 10 K/s. Water-cooled grips were placed 16 mm apart at both ends of the sample. A parabolic temperature distribution is established where the center is the hottest and both ends are at room temperature. A thermal equilibrium is obtained along the loading direction for approximately 3 mm at the center of the thermocouple. In this region deformation is localized and hence regarded as the gauge section. The strain measurement was employed by video extensometer based on digital image correlation method using an iMetrum Video Gauge software [46], where fine speckle patterns were generated by spaying high temperature paint on the specimen's surface prior each test. Deformation was made after one minute of isothermal holding at a strain rate approximately 10^{-3} s^{-1} and video data is stored at an acquisition frequency of 10 Hz and subsequently analyzed to trace speckle movement within the gauge. Since the testing was isothermal, the strain camera settings were adjusted to optimal imaging conditions prior each test to ensure speckle patterns are clearly visible even the material is glowing. The subsequent strain measurements were completed using the commercial software Video Gauge^{TM}, where a point-based approach was used to mimic traditional gauges. The above-mentioned experimental set-up was thoroughly documented in our previous work [46]. Both alloys were tested at 800, 900, 1000 and 1100 °C.

For cryogenic-temperature (-196°C) tensile test in the liquid nitrogen, $Hf_{15}Nb_{40}Ta_{25}Ti_{15}Zr_5$ RHEA samples were cut by EDM to dimensions of 17 (length) x 1.5 (width) x (0.5-0.7) (thickness) (mm^3). During the test, samples were rinsed in the liquid nitrogen, and an extensometer was employed to measure the strain. The strain rate was 10^{-3} s^{-1}.

2.3 Materials characterization

The microstructure and grain orientation of the RHEA samples were characterized by a field-emission scanning electron microscopy (SEM, FEI Quanta3D) equipped with Oxford Instruments EDS and EBSD detectors. The Oxford Aztec (Tango) software was employed to measure the misorientation between deformation twins or microbands and the matrix. In addition, a Rigaku XRD (Cu K_α radiation, Smartlab) was used to detect

phases. The microstructures were also characterized using a JEM-2100F transmission electron microscope (TEM) and a JEM-2800 TEM. Kernel average misorientation (KAM) maps for ultrafine grains and fine grains after tensile test at specific strains were achieved with the NanoMegas precession electron diffraction (PED) system that is installed in the JEM-2800 TEM. The TEM samples with a diameter of 3 mm were first mechanically ground to a thickness less than 50 μm. Then these discs were thinned through ion-milling to electron transparency using a Gatan PIPSII ion polishing system (Model 695).

2.4 Molecular dynamics (MD) simulation

A brick-shaped fragment of pure Nb is first created, with periodic boundary conditions along three orthogonal directions x = [100], y = [010], z = [001]. The initial aspect ratio of the brick-shaped configuration is 1:2:4, with dimensions ranging from $L_x \times L_y \times L_z$= 297A × 594A × 1188A (about 11 million atoms). To generate the alloying system, the Nb atoms are randomly selected and changed to Ta, Ti, which corresponds to an average composition $Nb_{60}Ta_{25}Ti_{15}$. 8 vacancy type prismatic loops (with burgers vectors of 1/2<111>) are inserted in to the Nb and $Nb_{60}Ta_{25}Ti_{15}$ system. We are using the embedded atom method (EAM) interatomic potentials developed by Zhou [47] and Lin [48] to model the interatomic interactions. The systems are compressed at a constant strain rate ($2e^9$ s^{-1}) along the [001] axis, under constant temperature (300K) using the isothermal, isobaric ensemble.

A second BCC simulation cell was created with three orthogonal axes along x = $[11\bar{2}]$, y = $[\bar{1}10]$, z= [111] with dimensions ranging from $L_x \times L_y \times L_z$ = 290A × 1160A × 580A. The procedures as aforementioned are applied. Crystals were compressed at a constant strain rate ($2e^9$ s^{-1}) along with the $[\bar{1}10]$ axis. Dislocation extraction algorithm (DXA) and grain segmentation algorithm (GSA) in OVITO are used to reveal structural defects in simulated crystals [49].

The finite-element modeling for the evolution of surface defects in samples during the cold-rolling step was employed. Two-dimensional model is set up in COMSOL Multiphysics 5.3. A flat-end rigid plate is in contact with the top surface of $Hf_{15}Nb_{40}Ta_{25}Ti_{15}Zr_5$. The width W and the height H of the $Hf_{15}Nb_{40}Ta_{25}Ti_{15}Zr_5$ are set to be 40 mm and 7.2 mm, respectively. A triangular defect is located on the center top

surface of the block. The bottom surface is fixed in the vertical direction; A downward vertical displacement is applied on the rigid plate. The contact between the indenter and $Hf_{15}Nb_{40}Ta_{25}Ti_{15}Zr_5$ is set to be frictionless. Before compression, the upper surface of the $Hf_{15}Nb_{40}Ta_{25}Ti_{15}Zr_5$ remains flat, and the rigid plate is contact with it with no applied force. Free Triangular mesh was employed. The material properties of $Hf_{15}Nb_{40}Ta_{25}Ti_{15}Zr_5$ are the same as the measurement data from tensile tests.

3. Results

3.1 Cold workability and related microstructure evolution

Our RHEA has a composition of $Hf_{15}Nb_{40}Ta_{25}Ti_{15}Zr_5$ (at %, termed as NTTHZ), is fabricated by arc-melting and can be cold-rolled directly from the as-cast state to a reduction in thickness (RIT) of over 90% without intermediate annealing, thus exhibiting excellent processability, as illustrated in Fig.1(a-d) and Fig. S1. Such super formability is like that of the homogenized HfNbTaTiZr RHEA [24][25][29]. In addition, based on the CALPHAD results (see Fig. 2), the melting point of the NTTHZ RHEA is over 200°C higher than that of the Senkov alloy, indicating higher strength at elevated temperatures [11]. We first found that the matrix composition $Nb_{60}Ta_{25}Ti_{15}$ shows exceptional formability, while the addition of Hf up to 15 at % maintains cold-workability of the matrix ($Hf_{15}Nb_{45}Ta_{25}Ti_{15}$), while simultaneously strengthening the matrix (see Fig. S2). The addition of Hf can help to decrease valence electron concentration value of alloys, which may contribute to improve ductility in BCC RHEAs [19]. In previous work, as-cast equiatomic NbTaTi alloy exhibits good tensile properties [18][21], indicating similar cold workability to the current non-equiatomic $Nb_{60}Ta_{25}Ti_{15}$ matrix. During the cold-work process for NTTHZ RHEA, surface defects formed during the previous solidification step that can be eliminated by the subsequent cold rolling step (as shown in Fig. 1b and Fig. 3a), meaning that this material self-heals effectively during processing. Finite-element modeling is employed to understand this defect elimination, as shown in Fig. 3b, where compression processing is treated as the primary deformation mode during cold rolling. It is found that the stress concentration at the surface defects is always lower than the tensile ultimate stress of the sample, which prevents the growth of surface cracks. On the

other hand, the tensile stress, caused by surface friction during the cold rolling step, helps to elongate samples mainly along the rolling direction, which makes surface cracks blunt progressively with increasing RIT. This behavior is unique, as other as-cast RHEAs with reasonable tensile ductility at ambient temperature[15] still fracture with RIT less than 40% (see Fig. S3), and also demonstrate lower fracture toughness than $Hf_{15}Nb_{40}Ta_{25}Ti_{15}Zr_5$ (see Fig. S4). In the cold rolling process for $Hf_{15}Nb_{40}Ta_{25}Ti_{15}Zr_5$, deformation-induced twins appear with RIT up to 60%, as shown in Fig.1(e-h). Similar deformation-induced twinning was reported during compression deformation of HfNbTaTiZr RHEA in the temperature range from room temperature to 600°C [50]. Some deformation-induced microbands or kink bands with misorientation less than 30° are also formed (see Fig.1h and Fig. S5) with RIT of 30% and 60%. When the RIT reaches 80%, some shear bands appear (see Fig. S6). Eventually, with a larger RIT of 91%, the surface defects completely disappear. The formation of deformation twins and deformation-induced microbands contribute to the suppression of surface crack propagation, which is similar to the effect of nano-twins on improving fracture resistance in the Cantor alloy at cryogenic temperatures [7].

With a RIT over 90%, some nano-scale bands with a high-density of dislocations appear (Fig. 1i), which are similar to lamella bands formed in severely cold-rolled FCC metals or alloys with high/medium stacking fault energies [51][52]. It is also interesting to note that the hardness of the sample maintains at a high value (~350 Vickers hardness) during the cold-rolling process when RIT is over 30% (see Fig. S7a), while the microhardness usually increases with RIT more rapidly for FCC HEAs with large RIT above this value. In addition, the microhardness of cold-rolled samples even slightly decreases when RIT increases from 30% to 60%, providing evidence of a softening phenomenon. Based on the misorientation profiles in Fig. 1(e-h), the deformation-induced twins with 60° misorientation are from the {112}<111> twin system, while those with approximately 50° misorientation are associated with the {332}<113> twin system. With RIT increasing from 30% to 60%, more and more deformation-induced kink bands are formed, while fewer twins are observed. These kink bands contribute to softening and formability of specimens via stress relaxation and crystal reorientation, which is also observed in β-Ti alloys, pure Ti, and the Senkov alloy [53][54][55][29].The phases present in the cold-rolled

$Hf_{15}Nb_{40}Ta_{25}Ti_{15}Zr_5$ RHEA were also checked after rolling, and it was confirmed that this alloy remained a single BCC structure (Fig. S7b). The microhardness development of the cold-rolled $Hf_{15}Nb_{40}Ta_{25}Ti_{15}Zr_5$ RHEA is like that of the Senkov alloy in the severe cold-rolled state, where further cold rolling (from RIT of 65% to RIT of 86%) did not result in significant additional changes in the Senkov alloy [24].

3.2 Tunable microstructure

Furthermore, the microstructure of the cold-rolled $Hf_{15}Nb_{40}Ta_{25}Ti_{15}Zr_5$ RHEA can be tailored by controlling the annealing conditions. After annealing at different temperatures for short times from 0.5 to 1 h, an HL structure (shown in Fig. 4a and 4b), fine grains (Fig. 5a and 5b) (FG, grain size~ 9.9 μm), and coarse grains (Fig. 5c and 5d) (CG, grain size~ 22.8 μm) can be formed inside $Hf_{15}Nb_{40}Ta_{25}Ti_{15}Zr_5$. The HL structure is composed of ultrafine-grained (UFG, grain size~ 0.7 μm) region and fine-grained (grain size~ 4.4 μm) region, where microhardness in the UFG area is much higher than that in FG area, as shown in Fig. S8. Due to the high-density of dislocations formed during severe cold rolling (Fig. 1i), atoms can diffuse along dislocations during annealing with a much higher diffusion rate (i.e., dislocation pipe diffusion rather than conventional lattice diffusion through a random walk mechanism[56][57]. Therefore, cold-rolled $Hf_{15}Nb_{40}Ta_{25}Ti_{15}Zr_5$ RHEA samples can be made homogeneous at a much lower annealing temperature (900 or 1150°C) and with shorter annealing times (1 h) (Fig. 4c and Fig. S9) when compared with conventional homogenization steps for RHEAs with the same matrix (Nb-25Ta-15Ti-based) (1500°C, over 12 h) (Fig. S10) or other similar RHEAs (HfNbTiTaZr, hot isostatically pressed for 2 h at 1200°C and then annealed at 1200°C for 24 h or annealed at 1800°C for 6-192 h) [25][58][29] in the as-cast state. This unique feature of the NTTHZ RHEA reported herein, saves both time and thermal energy during processing, greatly reduces the barrier for utilization of this alloy and consequently increases the potential for widespread industrial use.

3.3 Tensile properties in a broad temperature range

The $Hf_{15}Nb_{40}Ta_{25}Ti_{15}Zr_5$ RHEA alloys not only have excellent cold-workability in the as-cast state, but also good tensile strength-ductility synergy in the annealed state when tested at ambient-to-elevated temperatures. In the engineering stress-strain curves

shown in Fig. 6a, the $Hf_{15}Nb_{40}Ta_{25}Ti_{15}Zr_5$ RHEA with an HL structure can achieve a yield strength over 920 MPa and a failure elongation over 0.15 at room temperature, which is much stronger than the FG sample and at the same time remain as ductile as the CG sample. The mechanical properties of the FG and CG samples are similar to that of the as-cast NbHfTiZr RHEA [59]. The fracture surfaces of HL- NTTHZRHEA samples are presented in Fig. 6b and 6c, which clearly show transgranular ductile fracture. Fig. 7 shows the strain hardening rate curves for $Hf_{15}Nb_{40}Ta_{25}Ti_{15}Zr_5$ RHEA samples with different microstructures. Even with a finer heterogeneous structure and higher strength, the HL-NTTHZ specimens can maintain a high strain hardening rate that is similar to the CG specimens until fracture takes place.

4. Discussion

4.1 Deformation mechanism during cold rolling

Atomistic simulations of uniaxial compression along two different orientations, $[\bar{1}10]$ and [001] are performed to elucidate the deformation mechanisms in Nb-$Ta_{25}Ti_{15}$ alloy and pure Nb and understand the role of high concertation Ta and Ti solute atoms. When compressing along the $[\bar{1}10]$ direction, $Nb_{60}Ta_{25}Ti_{15}$ yields by deformation twinning, involving a reorientation of the crystal lattice within twinned volumes of the materials (Fig. 8a). Twin embryos nucleate right after yielding and grow rapidly with increasing the applied strain, which fills large fractions of material volume. For [001] orientation, deformation-twins also nucleate in $Nb_{60}Ta_{25}Ti_{15}$ but only grow to a certain size, as shown in Fig. 8b. They are constrained from further growth by the surrounding dense dislocation networks, in which the predominant deformation mechanism in the system is dislocation slip. The orientation-dependent twinning can be interpreted by the twinning mechanism that occurs due to shear in <111> directions on {112} planes, and the twinning stress resolved from the compressive loading is dependent on loading orientations. It is interesting to note that, when comparing with $Nb_{60}Ta_{25}Ti_{15,}$ twinning deformation and twin growth in pure Nb are drastically reduced, especially for [001] orientation compression, where stable twins do not occur (Fig. 8c). Compared with pure Nb, the abundant twins in Nb-$Ta_{25}Ti_{15}$ alloy signify the role of solutes in promoting twinning. This may originate from

the atomic misfit strain and solid solution strengthening, giving rise to plastic flow stress above the critical value for activating twinning deformation. It is noted that $Nb_{60}Ta_{25}Ti_{15}$ is our base alloy composition that shows exceptional formability. The aim of the atomistic simulation is to reveal the role of concentrated solid solutions (mixing of Nb, Ta, and Ti, the three base elements in our alloys) on deformation mechanisms by comparing them to pure Nb. As illustrated in Figure 8, the addition of Ta and Ti (i.e., $Nb_{60}Ta_{25}Ti_{15}$) promotes twinning deformation. It is reasonable to speculate that further addition of Hf and Zr would influence twinning as its effect on stacking faulty energy modulation. The relationship between composition, stacking faculty energy, and twinning propensity deserve further and careful study.

4.2 Comparison of mechanical property at elevated temperatures

In addition to room temperature performance, it is helpful to remember why RHEAs are intriguing in the first place: *the promise of great strength at high temperature*. Therefore, we compare the tensile strength of the $Hf_{15}Nb_{40}Ta_{25}Ti_{15}Zr_5$ RHEAs with Ni-based superalloys [60][61][62][63][64][65], refractory metals[61], and Nb-based and Ta-based refractory alloys[61][66] at elevated temperatures in Fig. 9, which further demonstrates the potential of our $Hf_{15}Nb_{40}Ta_{25}Ti_{15}Zr_5$ RHEA for high-temperature applications. When comparing with some most widely used Ni-based superalloys like Inconel 625 and Inconel 718 for disk use, the tensile strength of the $Hf_{15}Nb_{40}Ta_{25}Ti_{15}Zr_5$ RHEA is almost twice and three times higher at 900°C and 1000°C, respectively. In addition, although some Ni-based superalloys like Mar-247, CMSX-2, CMSX-4 and CMSX-10 which were designed for blade applications show exceptional strength below 1000°C, their strength drastically decreases once the temperatures are over 1000°C, which is shown as the blue oval in Fig. 9. The current NTTHZ RHEA shows comparable strength to those of CMSX-4 and CMSX-10 when the temperature reaches 1100°C. In the case of CMSX-4 and CMSX-10, a high content of Ta is added to strengthen the matrix and increase the volume fraction of γ' with $L1_2$ structure. W element is added to improve the thermal stability of the alloy and strengthen the matrix. Moreover, a considerable amount of expensive Re (3-7 wt.%) is added to ensure good mechanical properties at elevated temperatures. However, their

melting points (~1300°C) would limit their further use at elevated temperatures. As for the conventional refractory Nb or Ta-based alloys, the tensile strength of the NTTHZRHEA is still stronger than most of them in the elevated temperature range studied here. The Nb-based C-3009 shows small decrease at elevated temperatures due to the strong solid-solution strengthening caused by Hf and W, which is also attributing to its high melting point [11]. Similar case can be found in Ta-10W alloy. Apart from strength-ductility synergy at ambient-to-elevated temperatures, this NTTHZ RHEA exhibits ultrahigh yield strength (~1.4 GPa) and good ductility (uniform elongation ~ 0.1) at cryogenic temperature of -196°C, as shown in Fig. S11a. $Hf_{15}Nb_{40}Ta_{25}Ti_{15}Zr_5$ RHEA can retain their high strength at elevated temperatures and exhibit considerable ductility at cryogenic conditions, evading the strength–ductility trade-off, as exhibited in Fig. S11b. The elongation-at-failure of the current $Hf_{15}Nb_{40}Ta_{25}Ti_{15}Zr_5$ RHEA remains in excess of 10% for all testing conditions, which represents a notable accomplishment for RHEAs. Therefore, this strong and ductility RHEA can be used for applications in a wide operating temperature range. $Hf_{15}Nb_{40}Ta_{25}Ti_{15}Zr_5$ RHEA shows comparable tensile properties to HfNbTaTiZr RHEA from -196°C to ambient temperature [24][25][26][27][28][30][67], as shown in Supplementary Table 2. The melting point of $Hf_{15}Nb_{40}Ta_{25}Ti_{15}Zr_5$ is higher than that of HfNbTaTiZr RHEA, indicating better performance at elevated temperatures [11].

4.3 Deformation mechanism in heterogeneous-structured RHEAs

To elucidate the strengthening mechanisms that are responsible for the observed high strength and high ductility of $Hf_{15}Nb_{40}Ta_{25}Ti_{15}Zr_5$ RHEA with HL structure at ambient temperature, “loading-unloading-reloading” (LUR) cyclic tensile tests were conducted to calculate the internal back-stress, as shown in Fig. S12. Due to the existence of back-stress, the hysteresis loop increases with increasing strain, known as the Bauschinger effect [36]. Following the work of Wu et al., back-stress can be expressed as the average value of yield stresses during the unloading and reloading process [68]. Fig. S12b shows back-stress increases rapidly when plastic deformation occurs, and when comparing with effective stress, back-stress contributes more to strengthening. The precession electron diffraction (PED) image (Fig. 10a and Fig. 10b) taken from the deformed HL-NTTHZ sample with plastic strain of 0.05 clearly demonstrates grain misorientation, which is clear evidence of strain partitioning caused by the strain gradient between UFG and FG. Such

strain partitioning leads to the generation of dislocations in FG regions, and pile-ups of dislocations gives rise to work hardening by the combination of generating long-range back stresses and creating obstacles for slip [35]. The EBSD IPF image in Fig. 10c shows that most of fine grains are elongated when the HL specimen is applied with a global strain of 0.08. The true strain in each grain can be calculated from its aspect ratio α as $\varepsilon = (\frac{2}{3}) \ln \alpha$, where $\alpha = w/l$, w and l is the width and length of the fine grain, respectively [36]. The average true strain in fine grains is calculated as 0.36, as shown in Fig.10d. Meanwhile, most ultrafine grains remain equiaxed at the strain of 0.08 (see Fig. 10e). This difference in plastic strain between fine grains (strain = 0.36 > 0.08) and ultrafine grains (strain < 0.08) gives rise to plastic strain partitioning. The plastic deformation has to be continuous at the FG/UFG interfaces, which further causes strain gradient near these interfaces. Accommodation of such strain gradient requires the generation of geometrically necessary dislocations (GNDs) [69][70]. As a consequence, long-range back stresses are created and essentially work as a strain hardening mechanism. Microscopically, back-stress can be mapped indirectly by the density of GNDs, which can be computed from the lattice orientation gradients measured during post-deformed EBSD experiments [71][72]. GND density can be averaged for every grain to present the influence of the heterogeneous grain structure [73][74]. When comparing with GND density of samples before tensile deformation (see Fig. S13), a significant increase of GND density, approximately one order of magnitude higher, appears in the deformed HL specimen, as shown in Fig. 10f and 10g. The heterogeneous grain structure in Fig. 10f leads to considerably non-uniform distribution of local strain, which gives rise to the heterogeneity of GND density distribution. In Fig. 10g, yellow or red color representing high GND density that lies in the UFG domains, while a green coloring signifying low GND density primarily found in the FG regions, suggesting that FG areas undergo a relatively uniform strain with no large strain gradients along the interfaces. At the same time, ultrafine grains neighboring the UFG/FG boundaries undergo plastic deformation with higher geometric constraints, which leads to a higher strain gradient and higher GND density. However, some lamella composed of UFG act as coarse grains during the plastic deformation, where lower GND density is distributed. The above TEM PED work with kernel average misorientation map (KAM), TEM micrographs of dislocation distribution,

and the EBSD-based GND density calculation, confirm the effect of back-stress strengthening on the improvement of the mechanical properties of our HL- NTTHZRHEA specimen at different stages during plastic deformation. For $Hf_{15}Nb_{40}Ta_{25}Ti_{15}Zr_5$ RHEA samples tested at elevated temperatures, it is found that HL structure can be retained after tensile tests at 800°C and 900°C. However, the specimen is close to completed recrystallization after deformation at 1000°C, as shown in Fig. S14.

5. Conclusions

In summary, a novel refractory HEA was designed and fabricated, with excellent processibility that can be severely cold worked at room temperature directly from the as-cast state without intermediate annealing. The surface defects caused by the solidification can be eliminated by the cold rolling process itself. It is postulated that the deformation-induced twins and microbands formed during the cold-rolling process are responsible for this self-healing phenomenon. The formation mechanism of deformation-induced twins is confirmed by MD simulation analysis. The excellent cold-workability allows this RHEA to have tunable microstructure in the subsequent annealing step. Dislocation pipe diffusion significantly increases the diffusion rate, making this RHEA homogeneous in an energy and time efficient way, a true achievement for an ultra-high melting point alloy. We have also demonstrated experimentally that our $Hf_{15}Nb_{40}Ta_{25}Ti_{15}Zr_5$ RHEA is both strong and ductile at cryogenic-to-elevated temperatures. Back-stress strengthening contributes to the high tensile strength of hetero-structured $Hf_{15}Nb_{40}Ta_{25}Ti_{15}Zr_5$ RHEA at ambient temperature. Our NbTaTi-based refractory HEA design strategy provides a practical way to design and fabricate metallic materials with ultra-high melting points and excellent processibility.

Data availability

The data that support the findings of this study are available within the paper and the Supplementary Information, and all data are available from the authors on reasonable request.

References

[1] Y. Zhang, T.T. Zuo, Z. Tang, M.C. Gao, K.A. Dahmen, P.K. Liaw, Z.P. Lu, Microstructures and properties of high-entropy alloys, Prog. Mater. Sci. 61 (2014) 1–93.

[2] D.B. Miracle, O.N. Senkov, A critical review of high entropy alloys and related concepts, Acta Mater. 122 (2017) 448–511.

[3] E.P. George, D. Raabe, R.O. Ritchie, High-entropy alloys, Nat. Rev. Mater. (2019) 1.

[4] T. Yang, Y.L. Zhao, Y. Tong, Z.B. Jiao, J. Wei, J.X. Cai, X.D. Han, D. Chen, A. Hu, J.J. Kai, Multicomponent intermetallic nanoparticles and superb mechanical behaviors of complex alloys, Science (80-.). 362 (2018) 933–937.

[5] Z. Fu, L. Jiang, J.L. Wardini, B.E. MacDonald, H. Wen, W. Xiong, D. Zhang, Y. Zhou, T.J. Rupert, W. Chen, A high-entropy alloy with hierarchical nanoprecipitates and ultrahigh strength, Sci. Adv. 4 (2018) eaat8712.

[6] J.Y. He, H. Wang, H.L. Huang, X.D. Xu, M.W. Chen, Y. Wu, X.J. Liu, T.G. Nieh, K. An, Z.P. Lu, A precipitation-hardened high-entropy alloy with outstanding tensile properties, Acta Mater. 102 (2016) 187–196.

[7] B. Gludovatz, A. Hohenwarter, D. Catoor, E.H. Chang, E.P. George, R.O. Ritchie, A fracture-resistant high-entropy alloy for cryogenic applications, Science (80-.). 345 (2014) 1153–1158.

[8] O.N. Senkov, D.B. Miracle, K.J. Chaput, J.-P. Couzinie, Development and exploration of refractory high entropy alloys—A review, J. Mater. Res. 33 (2018) 3092–3128.

[9] C. Lee, G. Kim, Y. Chou, B.L. Musicó, M.C. Gao, K. An, G. Song, Y.-C. Chou, V. Keppens, W. Chen, Temperature dependence of elastic and plastic deformation behavior of a refractory high-entropy alloy, Sci. Adv. 6 (2020) eaaz4748.

[10] F. Maresca, W.A. Curtin, Mechanistic origin of high strength in refractory BCC high entropy alloys up to 1900K, Acta Mater. 182 (2020) 235–249.

[11] O.N. Senkov, S. Gorsse, D.B. Miracle, High temperature strength of refractory complex concentrated alloys, Acta Mater. (2019).

[12] Y. Zou, S. Maiti, W. Steurer, R. Spolenak, Size-dependent plasticity in an Nb25Mo25Ta25W25 refractory high-entropy alloy, Acta Mater. 65 (2014) 85–97.

[13] Y. Zou, H. Ma, R. Spolenak, Ultrastrong ductile and stable high-entropy alloys at small scales, Nat. Commun. 6 (2015) 1–8.

[14] S. Wei, S.J. Kim, J. Kang, Y. Zhang, Y. Zhang, T. Furuhara, E.S. Park, C.C. Tasan, Natural-mixing guided design of refractory high-entropy alloys with as-cast tensile ductility, Nat. Mater. (2020) 1–7.

[15] H. Huang, Y. Wu, J. He, H. Wang, X. Liu, K. An, W. Wu, Z. Lu, Phase-transformation ductilization of brittle high-entropy alloys via metastability engineering, Adv. Mater. 29 (2017) 1701678.

[16] O.N. Senkov, G.B. Wilks, D.B. Miracle, C.P. Chuang, P.K. Liaw, Refractory high-entropy alloys, Intermetallics. 18 (2010) 1758–1765.

[17] O.N. Senkov, D.B. Miracle, S.I. Rao, Correlations to improve room temperature ductility of refractory complex concentrated alloys, Mater. Sci. Eng. A. 820 (2021) 141512.

[18] Y.-C. Huang, Y.-C. Lai, Y.-H. Lin, S.-K. Wu, A study on the severely cold-rolled and annealed quaternary equiatomic derivatives from quinary HfNbTaTiZr refractory high entropy alloy, J. Alloys Compd. 855 (2021) 157404.

[19] S. Sheikh, S. Shafeie, Q. Hu, J. Ahlström, C. Persson, J. Veselý, J. Zýka, U. Klement, S. Guo, Alloy design for intrinsically ductile refractory high-entropy alloys, J. Appl. Phys. 120 (2016) 164902.

[20] L. Lilensten, J.-P. Couzinié, J. Bourgon, L. Perrière, G. Dirras, F. Prima, I. Guillot, Design and tensile properties of a bcc Ti-rich high-entropy alloy with transformation-induced plasticity, Mater. Res. Lett. 5 (2017) 110–116.

[21] S.-P. Wang, E. Ma, J. Xu, New ternary equi-atomic refractory medium-entropy alloys with tensile ductility: Hafnium versus titanium into NbTa-based solution, Intermetallics. 107 (2019) 15–23.

[22] J. Zýka, J. Málek, J. Veselý, F. Lukáč, J. Čížek, J. Kuriplach, O. Melikhova, Microstructure and room temperature mechanical properties of different 3 and 4 element medium entropy alloys from HfNbTaTiZr system, Entropy. 21 (2019) 114.

[23] Z. An, S. Mao, T. Yang, C.T. Liu, B. Zhang, E. Ma, H. Zhou, Z. Zhang, L. Wang, X. Han, Spinodal-modulated solid solution delivers a strong and ductile refractory high-entropy alloy, Mater. Horizons. 8 (2021) 948–955.

[24] O.N. Senkov, S.L. Semiatin, Microstructure and properties of a refractory high-entropy alloy after cold working, J. Alloys Compd. 649 (2015) 1110–1123.

[25] O.N. Senkov, A.L. Pilchak, S.L. Semiatin, Effect of cold deformation and annealing on the microstructure and tensile properties of a HfNbTaTiZr refractory high entropy alloy, Metall. Mater. Trans. A. 49 (2018) 2876–2892.

[26] S. Chen, K.-K. Tseng, Y. Tong, W. Li, C.-W. Tsai, J.-W. Yeh, P.K. Liaw, Grain growth and Hall-Petch relationship in a refractory HfNbTaZrTi high-entropy alloy, J. Alloys Compd. 795 (2019) 19–26.

[27] B. Schuh, B. Völker, J. Todt, N. Schell, L. Perrière, J. Li, J.P. Couzinié, A. Hohenwarter, Thermodynamic instability of a nanocrystalline, single-phase TiZrNbHfTa alloy and its impact on the mechanical properties, Acta Mater. 142 (2018) 201–212.

[28] C.-C. Juan, M.-H. Tsai, C.-W. Tsai, W.-L. Hsu, C.-M. Lin, S.-K. Chen, S.-J. Lin, J.-W. Yeh, Simultaneously increasing the strength and ductility of a refractory high-entropy alloy via grain refining, Mater. Lett. 184 (2016) 200–203.

[29] S. Zherebtsov, N. Yurchenko, D. Shaysultanov, M. Tikhonovsky, G. Salishchev, N. Stepanov, Microstructure and Mechanical Properties Evolution in HfNbTaTiZr Refractory High-Entropy Alloy During Cold Rolling, Adv. Eng. Mater. 22 (2020) 2000105.

[30] R.R. Eleti, N. Stepanov, S. Zherebtsov, Mechanical behavior and thermal activation analysis of HfNbTaTiZr body-centered cubic high-entropy alloy during tensile deformation at 77 K, Scr. Mater. 188 (2020) 118–123.

[31] F. Lukáč, M. Dudr, J. Čížek, P. Harcuba, T. Vlasák, M. Janeček, J. Kuriplach, J. Moon, H.S. Kim, J. Zýka, Defects in high entropy alloy HfNbTaTiZr prepared by high pressure torsion, Acta Phys. Pol., A. 134 (2018) 891–894.

[32] R.R. Eleti, V. Raju, M. Veerasham, S.R. Reddy, P.P. Bhattacharjee, Influence of strain on the formation of cold-rolling and grain growth textures of an equiatomic HfZrTiTaNb refractory high entropy alloy, Mater. Charact. 136 (2018) 286–292.

[33] J. Čížek, P. Haušild, M. Cieslar, O. Melikhova, T. Vlasák, M. Janeček, R. Král, P. Harcuba, F. Lukáč, J. Zýka, Strength enhancement of high entropy alloy HfNbTaTiZr by severe plastic deformation, J. Alloys Compd. 768 (2018) 924–937.

[34] Y. Zhu, K. Ameyama, P.M. Anderson, I.J. Beyerlein, H. Gao, H.S. Kim, E. Lavernia, S. Mathaudhu, H. Mughrabi, R.O. Ritchie, Heterostructured materials: superior properties from hetero-zone interaction, Mater. Res. Lett. 9 (2021) 1–31.

[35] E. Ma, T. Zhu, Towards strength–ductility synergy through the design of heterogeneous nanostructures in metals, Mater. Today. 20 (2017) 323–331.

[36] X. Wu, M. Yang, F. Yuan, G. Wu, Y. Wei, X. Huang, Y. Zhu, Heterogeneous lamella structure unites ultrafine-grain strength with coarse-grain ductility, Proc. Natl. Acad. Sci. 112 (2015) 14501–14505.

[37] Y. Wang, M. Chen, F. Zhou, E. Ma, High tensile ductility in a nanostructured metal, Nature. 419 (2002) 912.

[38] V.L. Tellkamp, E.J. Lavernia, A. Melmed, Mechanical behavior and microstructure of a thermally stable bulk nanostructured Al alloy, Metall. Mater. Trans. A. 32 (2001) 2335–2343.

[39] K. Lu, Making strong nanomaterials ductile with gradients, Science (80-.). 345 (2014) 1455–1456.

[40] Z. Cheng, H. Zhou, Q. Lu, H. Gao, L. Lu, Extra strengthening and work hardening in gradient nanotwinned metals, Science (80-.). 362 (2018) eaau1925.

[41] E. Ma, X. Wu, Tailoring heterogeneities in high-entropy alloys to promote strength–ductility synergy, Nat. Commun. 10 (2019) 1–10.

[42] C. Zhang, C. Zhu, T. Harrington, K. Vecchio, Design of non-equiatomic high entropy alloys with heterogeneous lamella structure towards strength-ductility synergy, Scr. Mater. 154 (2018) 78–82.

[43] C. Zhang, C. Zhu, P. Cao, X. Wang, F. Ye, K. Kaufmann, L. Casalena, B.E. MacDonald, X. Pan, K. Vecchio, E.J. Lavernia, Aged metastable high-entropy alloys with heterogeneous lamella structure for superior strength-ductility synergy, Acta Mater. 199 (2020) 602–612.

[44] Y. Murakami, Stress intensity factors, (1987).

[45] F. Jiang, K.S. Vecchio, Fracture of Nitinol under quasistatic and dynamic loading, Metall. Mater. Trans. A. 38 (2007) 2907–2915.

[46] S. Sulzer, E. Alabort, A. Németh, B. Roebuck, R. Reed, On the rapid assessment of mechanical behavior of a prototype nickel-based superalloy using small-scale testing, Metall. Mater. Trans. A. 49 (2018) 4214–4235.

[47] X.W. Zhou, R.A. Johnson, H.N.G. Wadley, Misfit-energy-increasing dislocations in vapor-deposited CoFe/NiFe multilayers, Phys. Rev. B. 69 (2004) 144113.

[48] D.-Y. Lin, S.S. Wang, D.L. Peng, M. Li, X.D. Hui, An n-body potential for a Zr–Nb system based on the embedded-atom method, J. Phys. Condens. Matter. 25 (2013) 105404.

[49] A. Stukowski, Visualization and analysis of atomistic simulation data with OVITO–the Open Visualization Tool, Model. Simul. Mater. Sci. Eng. 18 (2009) 15012.

[50] O.N. Senkov, J.M. Scott, S. V Senkova, F. Meisenkothen, D.B. Miracle, C.F. Woodward, Microstructure and elevated temperature properties of a refractory TaNbHfZrTi alloy, J. Mater. Sci. 47 (2012) 4062–4074.

[51] C. Zhang, C. Zhu, K. Vecchio, Non-equiatomic FeNiCoAl-based high entropy alloys with multiscale heterogeneous lamella structure for strength and ductility, Mater. Sci. Eng. A. 743 (2019) 361–371.

[52] D.A. Hughes, N. Hansen, Microstructure and strength of nickel at large strains, Acta Mater. 48 (2000) 2985–3004.

[53] S. Sadeghpour, S.M. Abbasi, M. Morakabati, L.P. Karjalainen, Effect of dislocation channeling and kink band formation on enhanced tensile properties of a new beta Ti alloy, J. Alloys Compd. 808 (2019) 151741.

[54] Y. Yang, S.Q. Wu, G.P. Li, Y.L. Li, Y.F. Lu, K. Yang, P. Ge, Evolution of deformation mechanisms of Ti–22.4 Nb–0.73 Ta–2Zr–1.34 O alloy during straining, Acta Mater. 58 (2010) 2778–2787.

[55] A.T. Churchman, The yield phenomena, kink bands and geometric softening in titanium crystals, Acta Metall. 3 (1955) 22–29.

[56] P. Shewmon, Diffusion in solids, Springer, 2016.

[57] Z. Balogh, G. Schmitz, Diffusion in metals and alloys, in: Phys. Metall., Elsevier, 2014: pp. 387–559.

[58] S. Maiti, W. Steurer, Structural-disorder and its effect on mechanical properties in single-phase TaNbHfZr high-entropy alloy, Acta Mater. 106 (2016) 87–97.

[59] Z. Lei, X. Liu, Y. Wu, H. Wang, S. Jiang, S. Wang, X. Hui, Y. Wu, B. Gault, P. Kontis, Enhanced strength and ductility in a high-entropy alloy via ordered oxygen complexes, Nature. 563 (2018) 546.

[60] R.C. Reed, The superalloys: fundamentals and applications, Cambridge university press, 2008.

[61] N.E. Prasad, R.J.H. Wanhill, Aerospace materials and material technologies, Springer, 2017.

[62] M. Kaufman, Properties of cast Mar-M-247 for turbine blisk applications, Superalloys 1984. (1984) 43–52.

[63] A. Sengupta, S.K. Putatunda, L. Bartosiewicz, J. Hangas, P.J. Nailos, M. Peputapeck,

F.E. Alberts, Tensile behavior of a new single-crystal nickel-based superalloy (CMSX-4) at room and elevated temperatures, J. Mater. Eng. Perform. 3 (1994) 73–81.

[64] G.L. Erickson, The development and application of CMSX-10, Superalloys. 1996 (1996) 35–44.

[65] S. Wee, J. Do, K. Kim, C. Lee, C. Seok, B.-G. Choi, Y. Choi, W. Kim, Review on mechanical thermal properties of superalloys and thermal barrier coating used in gas turbines, Appl. Sci. 10 (2020) 5476.

[66] C.C. Wojcik, W. Chang, Thermomechanical processing and properties of niobium alloys., in: Int. Symp. Niobium 2001, 2001: pp. 163–173.

[67] S. Wang, M. Wu, D. Shu, G. Zhu, D. Wang, B. Sun, Mechanical instability and tensile properties of TiZrHfNbTa high entropy alloy at cryogenic temperatures, Acta Mater. 201 (2020) 517–527.

[68] M. Yang, Y. Pan, F. Yuan, Y. Zhu, X. Wu, Back stress strengthening and strain hardening in gradient structure, Mater. Res. Lett. 4 (2016) 145–151.

[69] M.F. Ashby, The deformation of plastically non-homogeneous materials, Philos. Mag. 21 (1970) 399–424.

[70] H. Gao, Y. Huang, Geometrically necessary dislocation and size-dependent plasticity, Scr. Mater. 48 (2003) 113–118.

[71] C. Zhu, T. Harrington, V. Livescu, G.T. Gray, K.S. Vecchio, Determination of geometrically necessary dislocations in large shear strain localization in aluminum, Acta Mater. 118 (2016) 383–394.

[72] C. Zhu, T. Harrington, G.T. Gray, K.S. Vecchio, Dislocation-Type Evolution in Quasi-Statically Compressed Polycrystalline Nickel, Acta Mater. (2018).

[73] C. Zhu, V. Livescu, T. Harrington, O. Dippo, G.T. Gray, K.S. Vecchio, Investigation of the shear response and geometrically necessary dislocation densities in shear localization in high-purity titanium, Int. J. Plast. 92 (2017) 148–163.

[74] E. Demir, D. Raabe, N. Zaafarani, S. Zaefferer, Investigation of the indentation size effect through the measurement of the geometrically necessary dislocations beneath small indents of different depths using EBSD tomography, Acta Mater. 57 (2009) 559–569.

Acknowledgements

C.Z., BEM and E.J.L. would like to acknowledge financial support from UCI. This research was also partially supported (EJL, X.W., BEM and TJR) by the National Science Foundation Materials Research Science and Engineering Center program through the UC Irvine Center for Complex and Active Materials (DMR-2011967). Xinyi W. and P.C. acknowledge financial support from National Science Foundation (DMR-2105328, CMMI-1935371). We also would like to thank Dr. Fan Ye, Dr. Li. Xing, and Dr. Jian-guo Zheng

(IMRI, UC Irvine) for TEM assistance. We acknowledge Dr. Mingde Qin and Xiao Liu (UC San Diego) for assistance in some experiments.

Competing interests

The authors declare no competing interests.

Figures

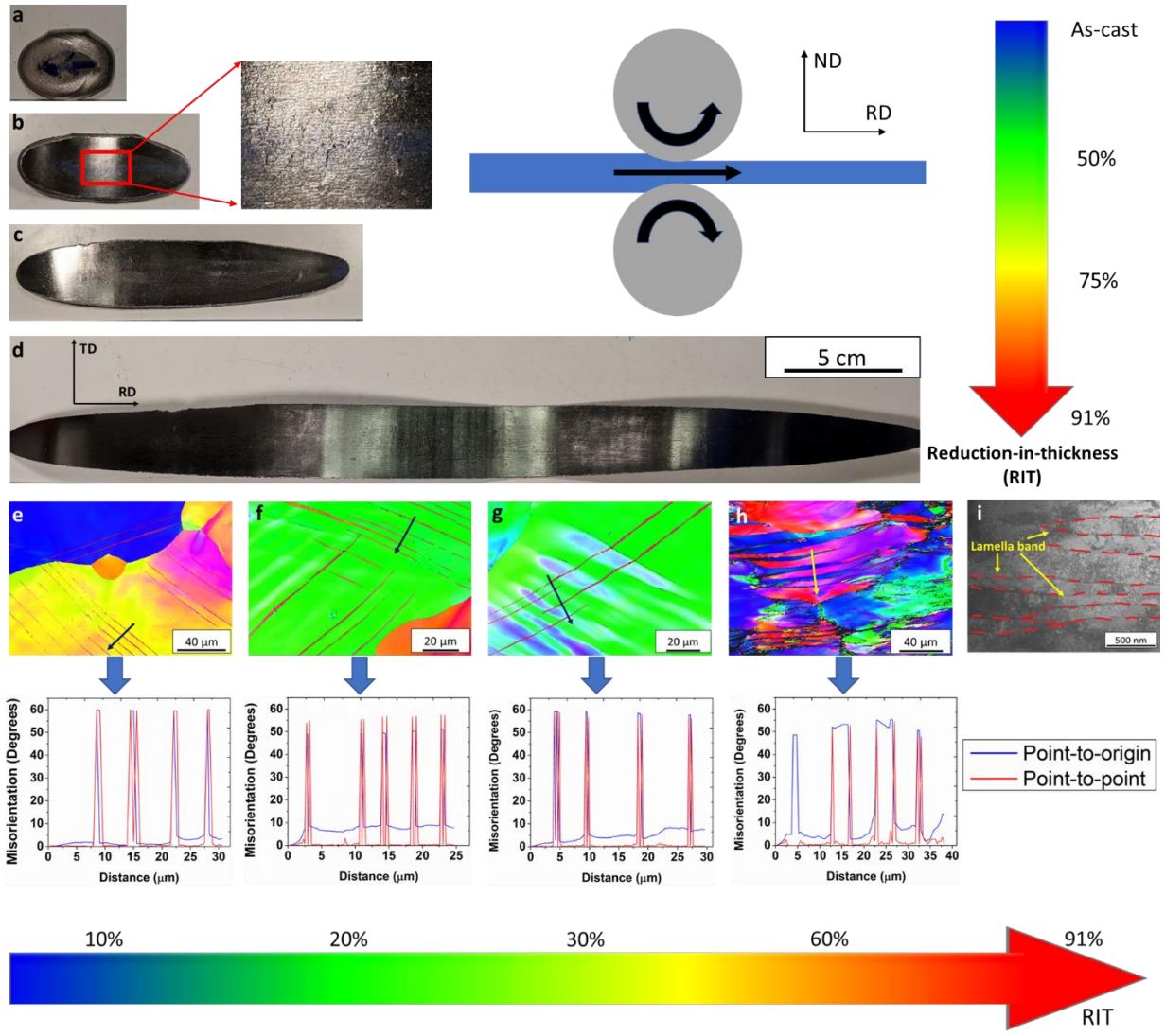

Fig. 1. Excellent cold-workability and the related deformed microstructure of $Hf_{15}Nb_{40}Ta_{25}Ti_{15}Zr_5$ RHEA at room temperature. Images of $Hf_{15}Nb_{40}Ta_{25}Ti_{15}Zr_5$ RHEA from (a) as-cast state to a reduction in thickness (RIT) of (b) 50% (some surface defects appear) (c) 75% and (d) 91%. Electron backscatter diffraction (EBSD) inverse pole figures (IPF) and related misorientation profiles of cold-rolled $Hf_{15}Nb_{40}Ta_{25}Ti_{15}Zr_5$ RHEA with RIT of (e) 10%, (f) 20%, (g) 30%, and (h) 60%. (i) Transmission electron microscopy (TEM) bright field (BF) micrograph of lamella bands with a high density of dislocations in NTTHZ RHEA with RIT of 91%. RD – rolling direction, ND- normal direction, TD – transverse direction.

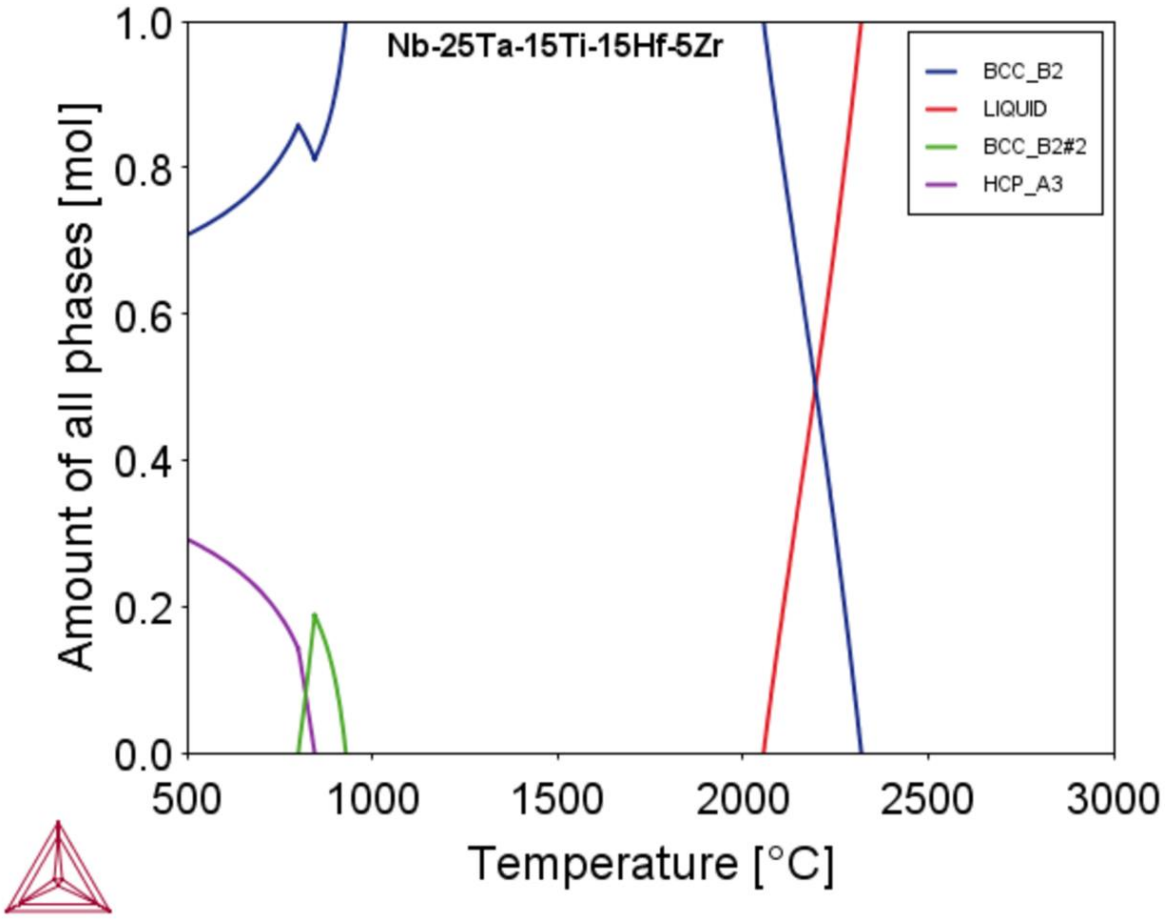

Fig. 2. CALPHAD result for $Hf_{15}Nb_{40}Ta_{25}Ti_{15}Zr_5$ RHEA, showing a high melting point around 2400°C.

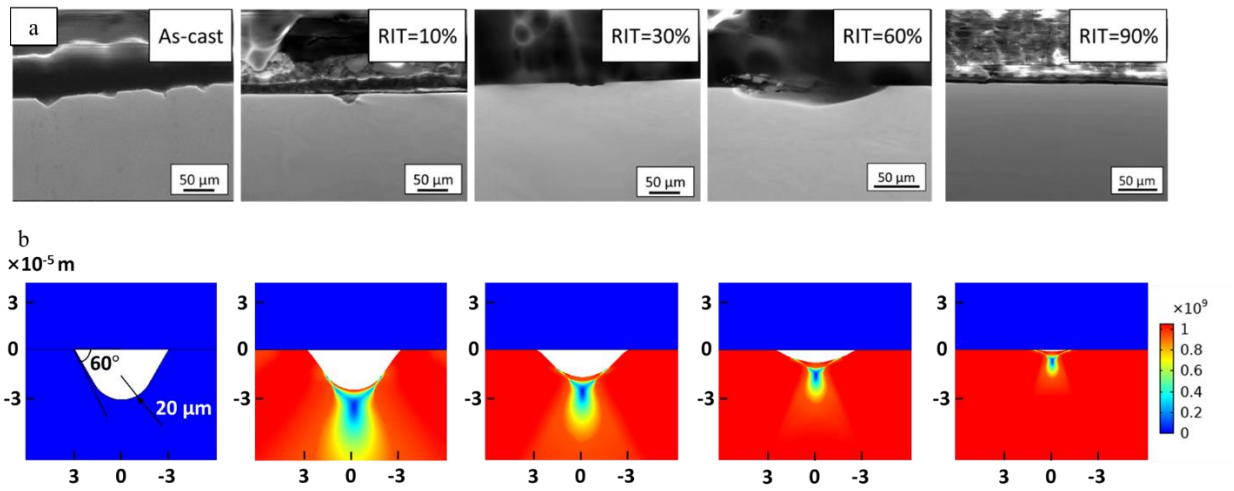

Fig. 3. Surface development of cold-rolled $Hf_{15}Nb_{40}Ta_{25}Ti_{15}Zr_5$ and related finite-element (FE) modeling, showing a unique process-healing phenomenon. (a) Evolution of surface defects in cold-rolled $Hf_{15}Nb_{40}Ta_{25}Ti_{15}Zr_5$ RHEA from the as-cast state to a RIT of 90%. (b) FE modeling for stress applied in the tip area of defects, unit: Pa.

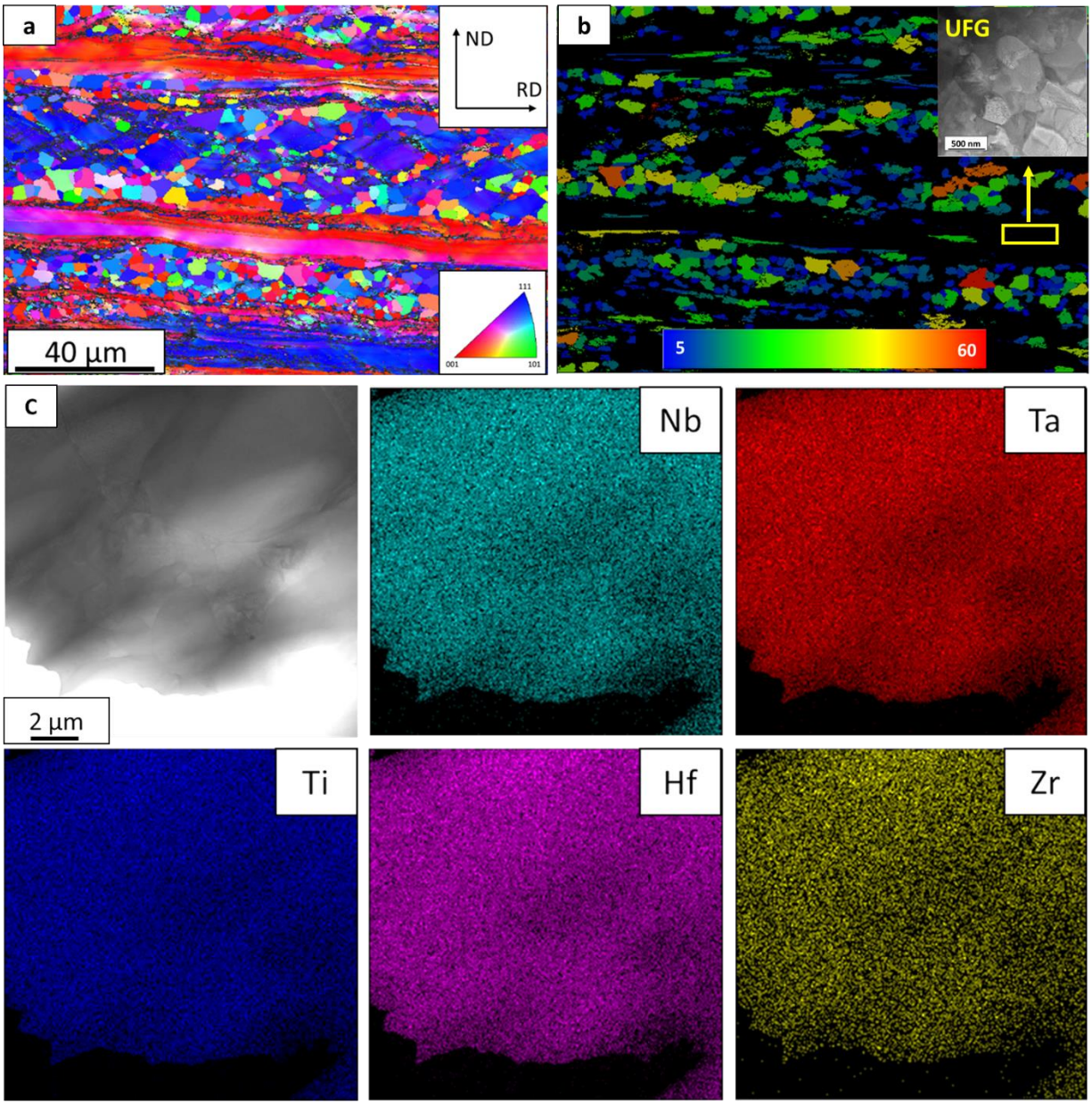

Fig. 4. Microstructure and related element distribution in $Hf_{15}Nb_{40}Ta_{25}Ti_{15}Zr_5$ RHEA with heterogeneous lamella (HL) structure. (a) EBSD inverse pole figure of $Hf_{15}Nb_{40}Ta_{25}Ti_{15}Zr_5$ RHEA after cold rolling with RIT of 90% and annealing at 900°C for 1 hour. (b) Corresponding grain area map of fully-recrystallized fine grains with grain area larger than 5 μm^2. Ultrafine grains (UFGs) in the recovery state are distributed in the black areas. (c) Scanning TEM micrograph and related EDS mapping of ultrafine and fine grains in the rolled and annealed $Hf_{15}Nb_{40}Ta_{25}Ti_{15}Zr_5$, showing no element segregation. RD – rolling direction, ND – normal direction.

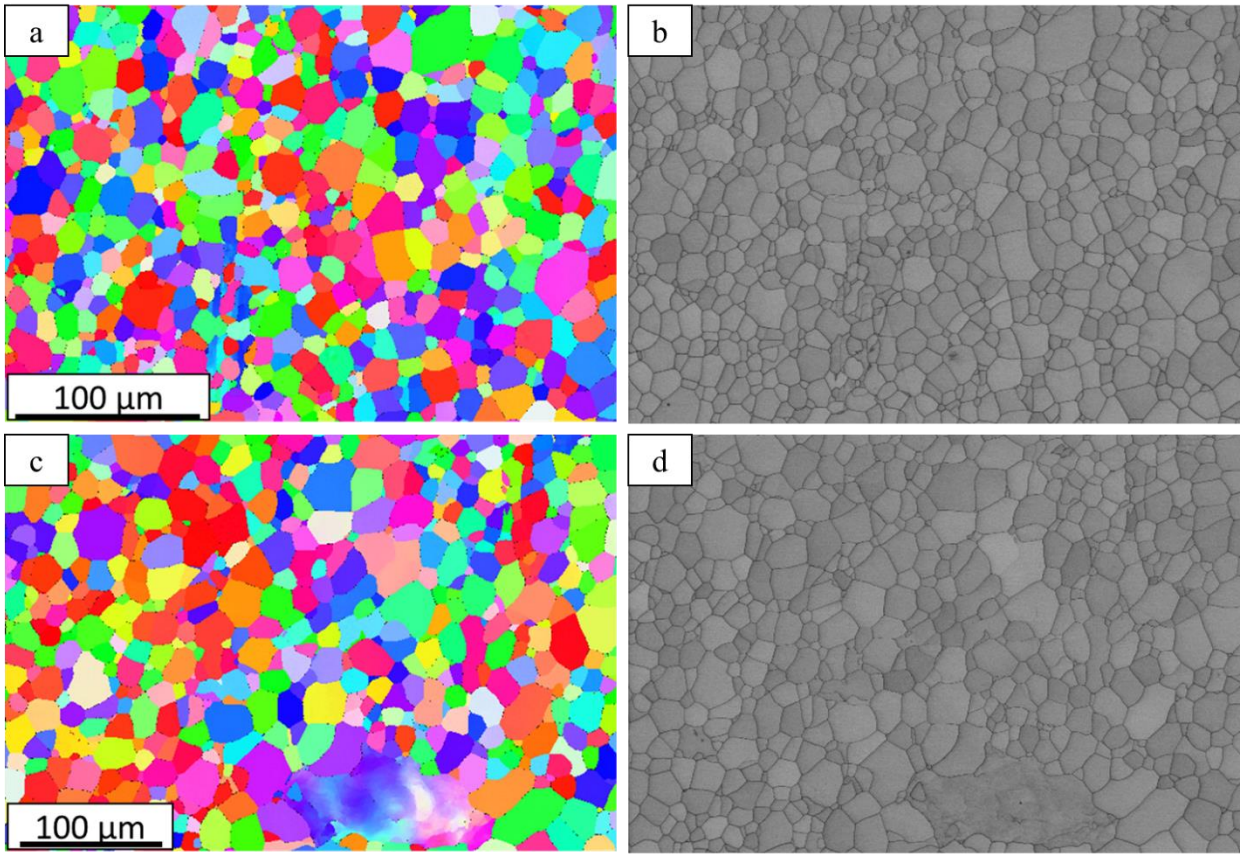

Fig. 5. EBSD inverse pole figures and related band contrast images for cold-rolled $Hf_{15}Nb_{40}Ta_{25}Ti_{15}Zr_5$ RHEA with different microstructures after annealing at different conditions. (a) EBSD IPF for CR90 $Hf_{15}Nb_{40}Ta_{25}Ti_{15}Zr_5$ RHEA after annealing at 1150°C for 1 h. (b) Related EBSD BC image for (a), showing a fine-grained microstructure. (c) EBSD IPF for CR90 $Hf_{15}Nb_{40}Ta_{25}Ti_{15}Zr_5$ RHEA after annealing at 1300°C for 0.5 h. (d) Related EBSD BC image for (c), showing a coarse-grained microstructure.

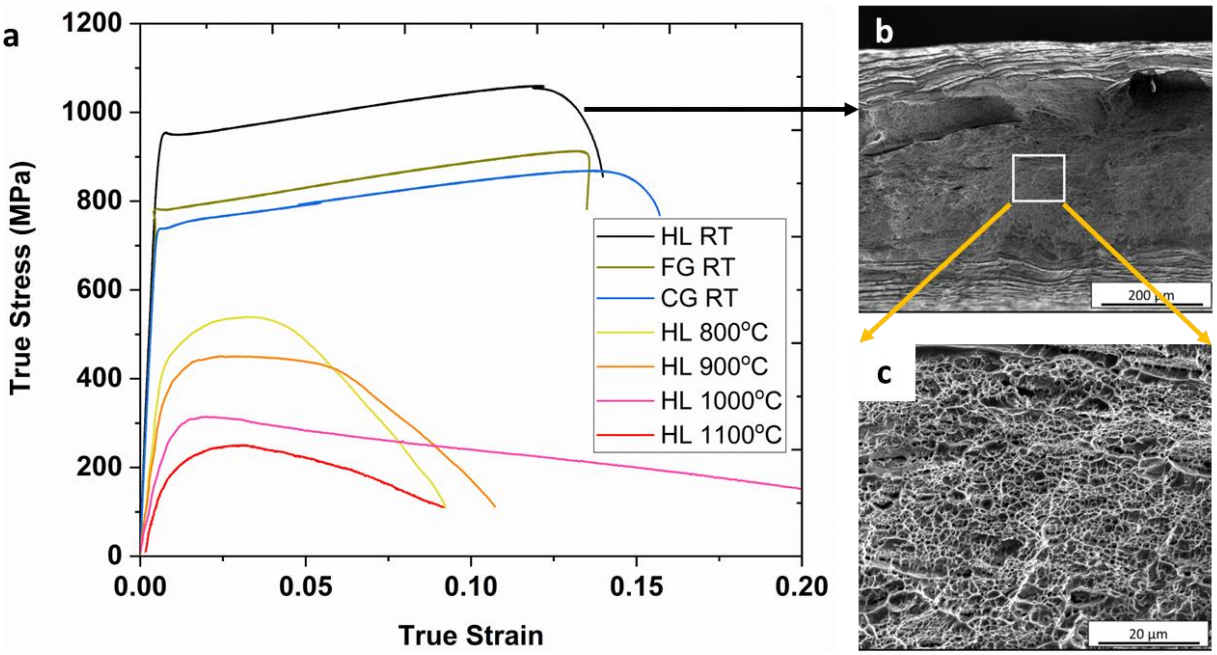

Fig. 6. High tensile strength-ductility synergy achieved in $Hf_{15}Nb_{40}Ta_{25}Ti_{15}Zr_5$ RHEA with HL structure at ambient-to-elevated temperatures. (a) Engineering stress-strain (SS) curves of $Hf_{15}Nb_{40}Ta_{25}Ti_{15}Zr_5$ RHEA with HL structure at ambient temperature and elevated temperatures (800°C, 900°C, 1000°C and 1100°C). Related SS curves of specimens with fine grains (FG) and coarse grains (CG) tested at room temperature are also shown. **SEM micrographs for the fracture surfaces of HL- NTTHZ RHEA after tensile test at room temperature**, showing a high density of dimples and ductile fracture type in (b) and (c).

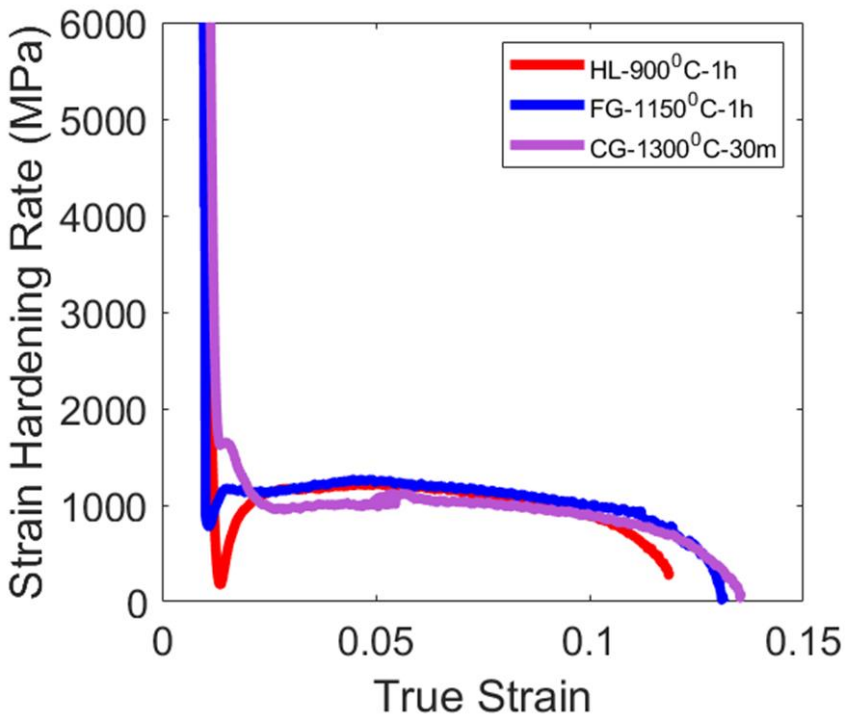

Fig. 7. Strain hardening rate curves of $Hf_{15}Nb_{40}Ta_{25}Ti_{15}Zr_5$ RHEA with different microstructures tested at room temperature.

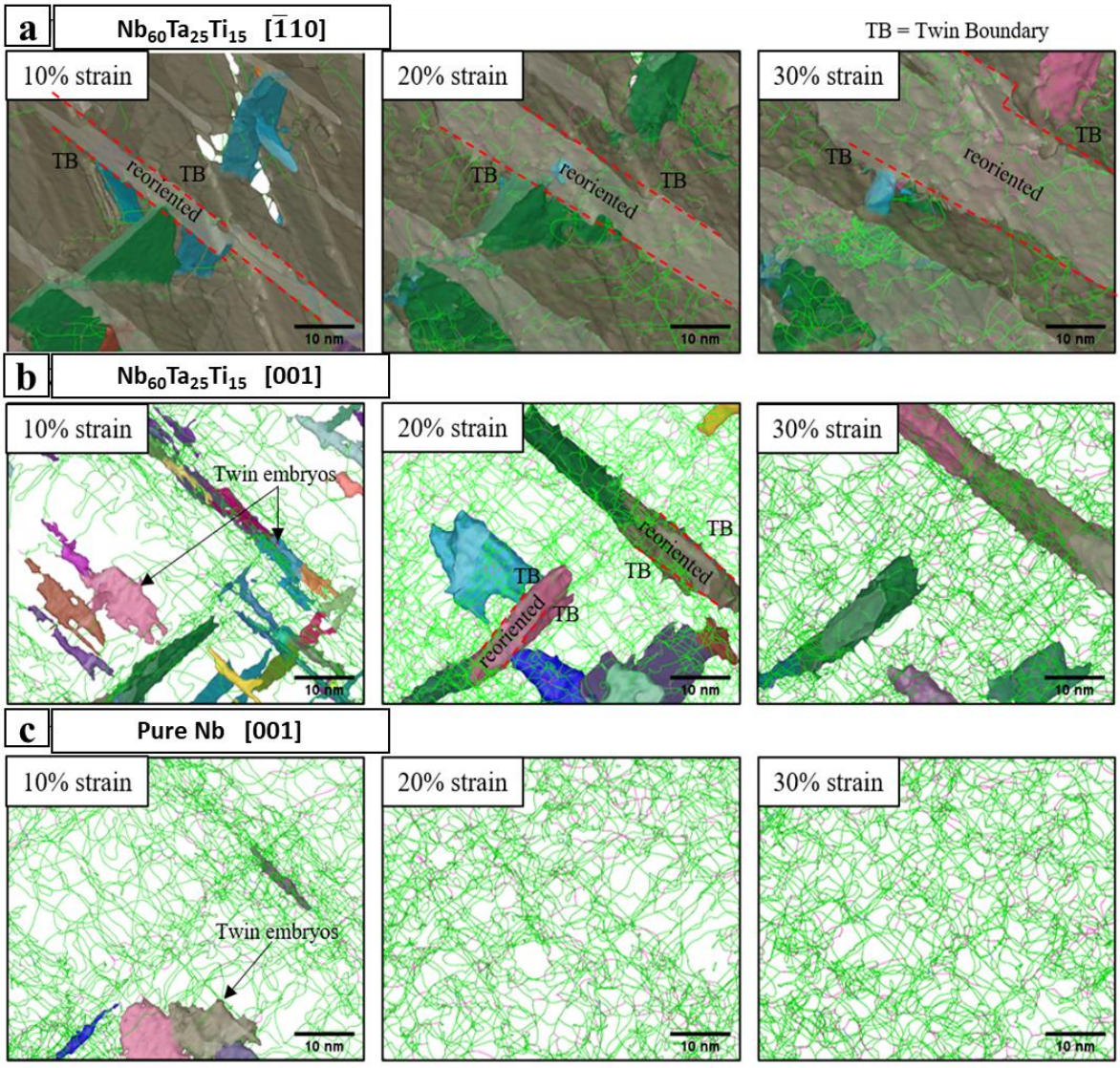

Fig. 8. Structural evolution response to compression. (a) $Nb_{60}Ta_{25}Ti_{15}$ under compression along [$\bar{1}$10] direction at 10% strain, 20% strain, 30% strain respectively. From left to right, nucleation of twin embryos, twin propagation, and twin growth to span the simulation volume. (b) $Nb_{60}Ta_{25}Ti_{15}$ under compression along [001] direction. Twin embryos and twin growth within $Nb_{60}Ta_{25}Ti_{15}$. (c) pure Nb under compression along [001] direction, deformation governed by pure dislocation slip. Dislocations appear as green and magenta lines. The twins appear as surface mesh. Different colors represent different lattice orientations generated by grain segmentation algorithm in OVITO.

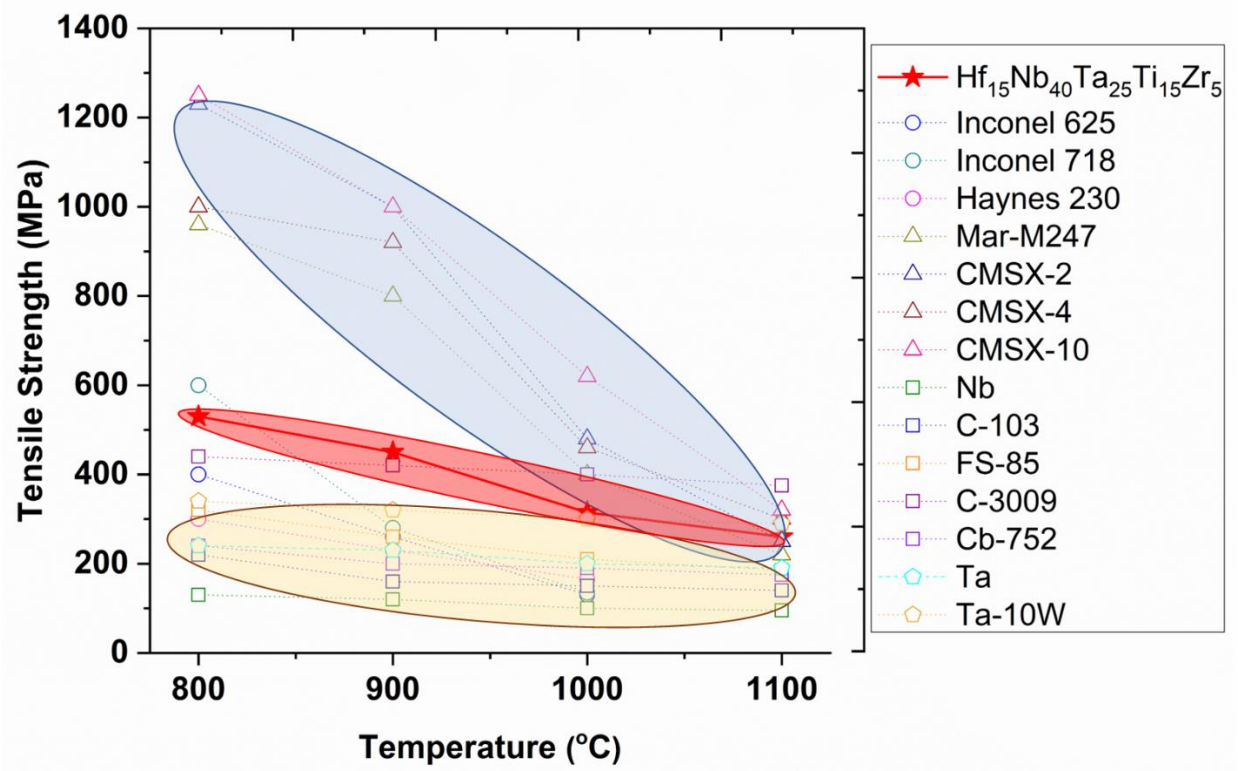

Fig. 9. Tensile strength versus the testing temperatures of $Hf_{15}Nb_{40}Ta_{25}Ti_{15}Zr_5$ with HL structure compared with those of ductile high-temperature metals and alloys, including conventional Ni-based superalloys [60-65], refractory metals (Nb, Ta) [61], and refractory Nb-based alloys and Ta-based alloys [61,66]. Blue and yellow shadow is for the strength range of superalloys (blade use) and refractory metallic materials at elevated temperatures, respectively.

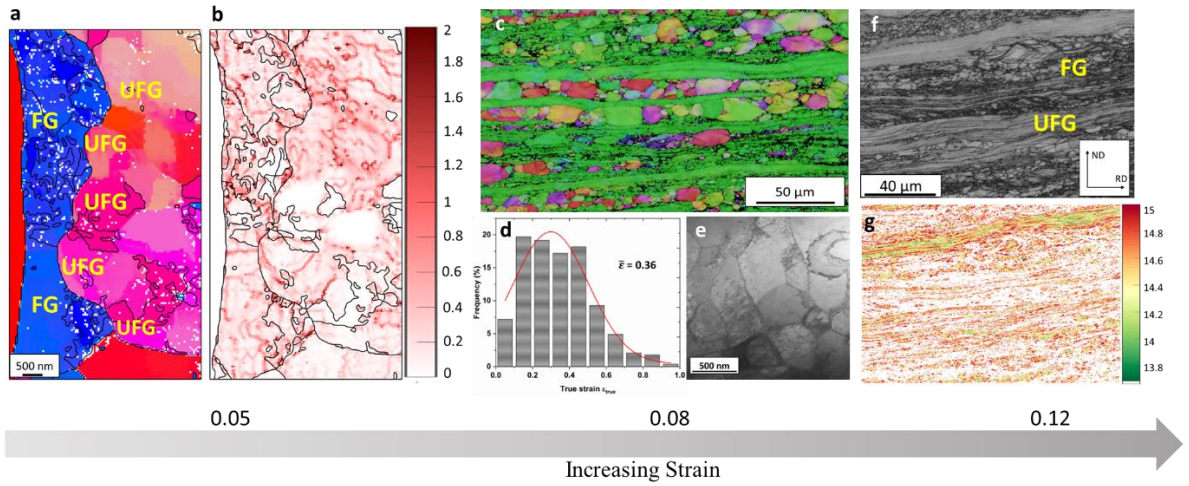

Fig. 10. Deformation mechanisms of $Hf_{15}Nb_{40}Ta_{25}Ti_{15}Zr_5$ RHEA with HL structure at different plastic stages. (a) TEM precession electron diffraction (PED) IPF for deformed $Hf_{15}Nb_{40}Ta_{25}Ti_{15}Zr_5$ RHEA with strain of 0.05. (b) Corresponding kernel average misorientation map (KAM) taken from the deformed specimen in (a), showing a higher strain localization and stronger dislocation activities along interfaces, unit: degree; (c) EBSD IPF image showing most fine grains are elongated along tensile direction at a strain of 0.08; (d) Distribution of strains in fine grains with an average true strain of 0.36 when the HL specimen is deformed to a strain of 0.08; (e) TEM micrograph showing equiaxed ultrafine grains in the HL specimen with a strain of 0.08; (f) EBSD band contrast (BC) micrograph of $Hf_{15}Nb_{40}Ta_{25}Ti_{15}Zr_5$ with strain of 0.12. (g) EBSD-based grain average GND density map corresponding to (D), showing a significant heterogeneous distribution of dislocation density, unit: $\log_{10}(m^{-2})$.

Figures

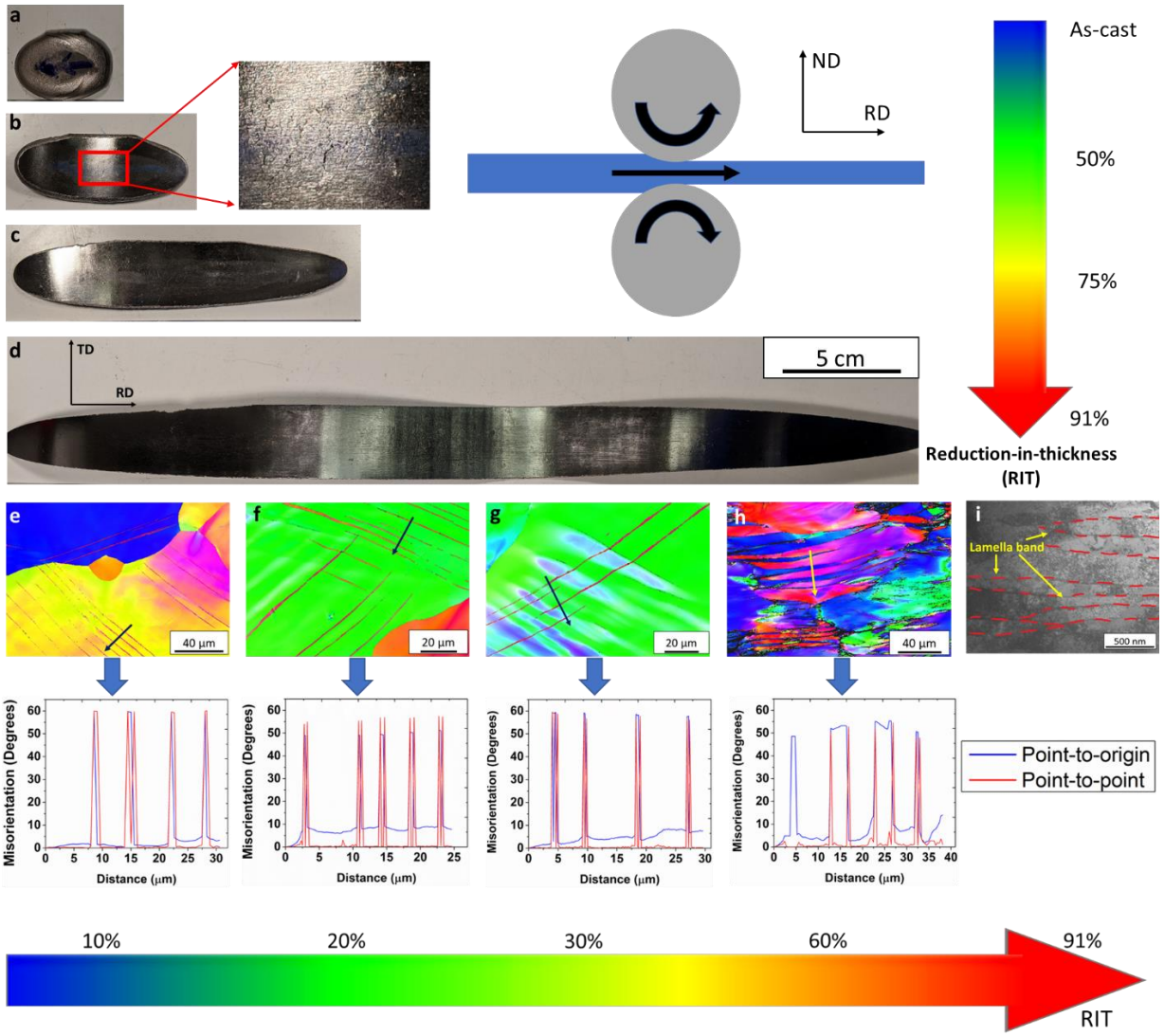

Fig. 1. Excellent cold-workability and the related deformed microstructure of $Hf_{15}Nb_{40}Ta_{25}Ti_{15}Zr_5$ RHEA at room temperature. Images of $Hf_{15}Nb_{40}Ta_{25}Ti_{15}Zr_5$ RHEA from (a) as-cast state to a reduction in thickness (RIT) of (b) 50% (some surface defects appear) (c) 75% and (d) 91%. Electron backscatter diffraction (EBSD) inverse pole figures (IPF) and related misorientation profiles of cold-rolled $Hf_{15}Nb_{40}Ta_{25}Ti_{15}Zr_5$ RHEA with RIT of (e) 10%, (f) 20%, (g) 30%, and (h) 60%. (i) Transmission electron microscopy (TEM) bright field (BF) micrograph of lamella bands with a high density of dislocations in NTTHZ RHEA with RIT of 91%. RD – rolling direction, ND- normal direction, TD – transverse direction.

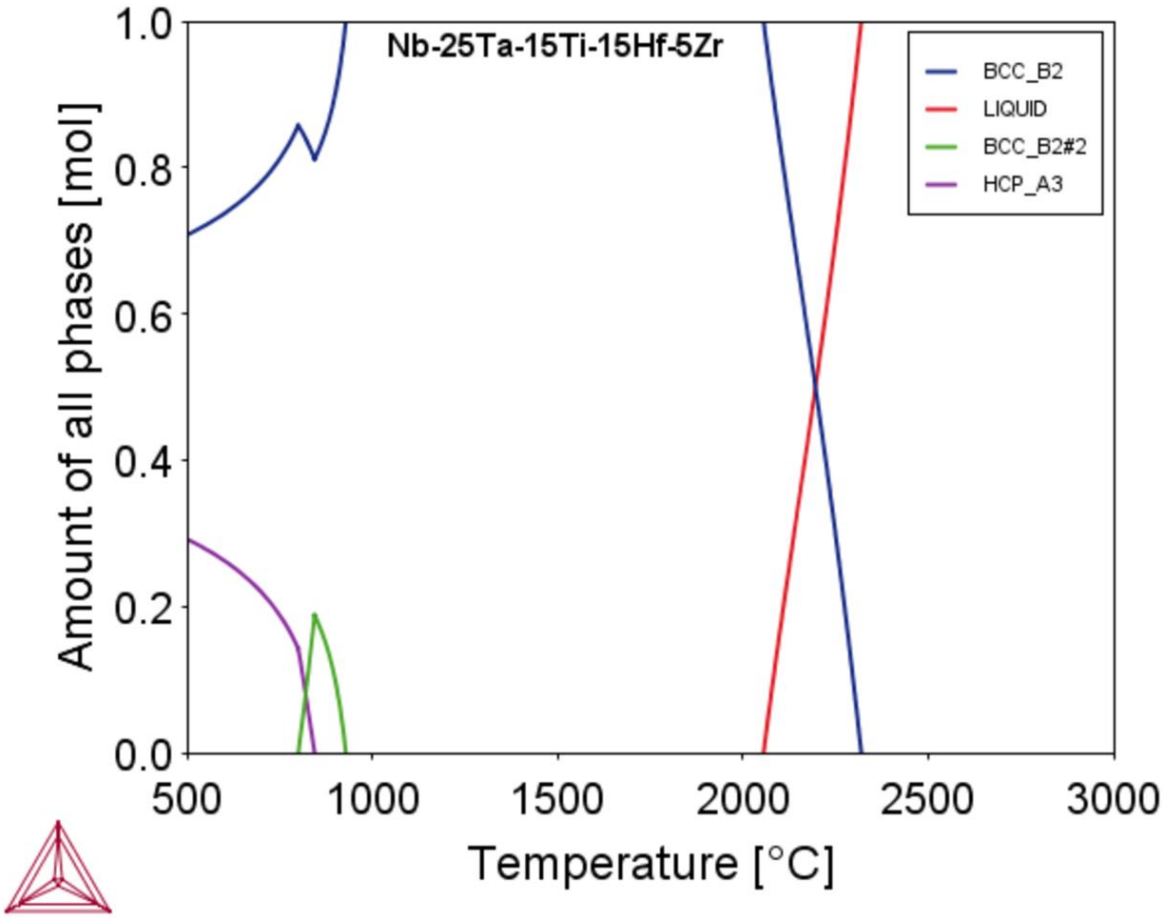

Fig. 2. CALPHAD result for $Hf_{15}Nb_{40}Ta_{25}Ti_{15}Zr_5$ RHEA, showing a high melting point around 2400°C.

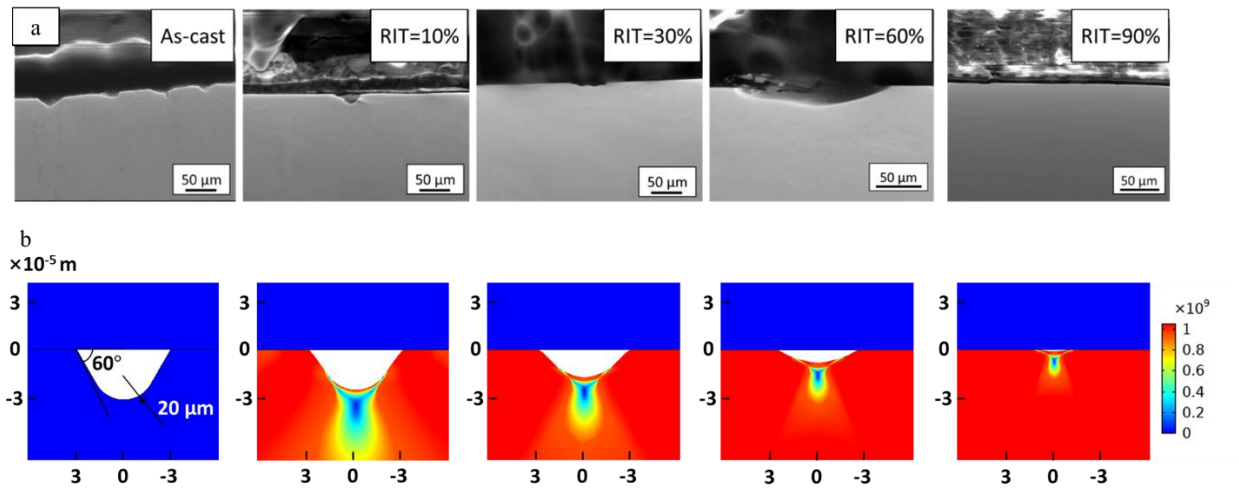

Fig. 3. Surface development of cold-rolled $Hf_{15}Nb_{40}Ta_{25}Ti_{15}Zr_5$ and related finite-element (FE) modeling, showing a unique process-healing phenomenon. (a) Evolution of surface defects in cold-rolled $Hf_{15}Nb_{40}Ta_{25}Ti_{15}Zr_5$ RHEA from the as-cast state to a RIT of 90%. (b) FE modeling for stress applied in the tip area of defects, unit: Pa.

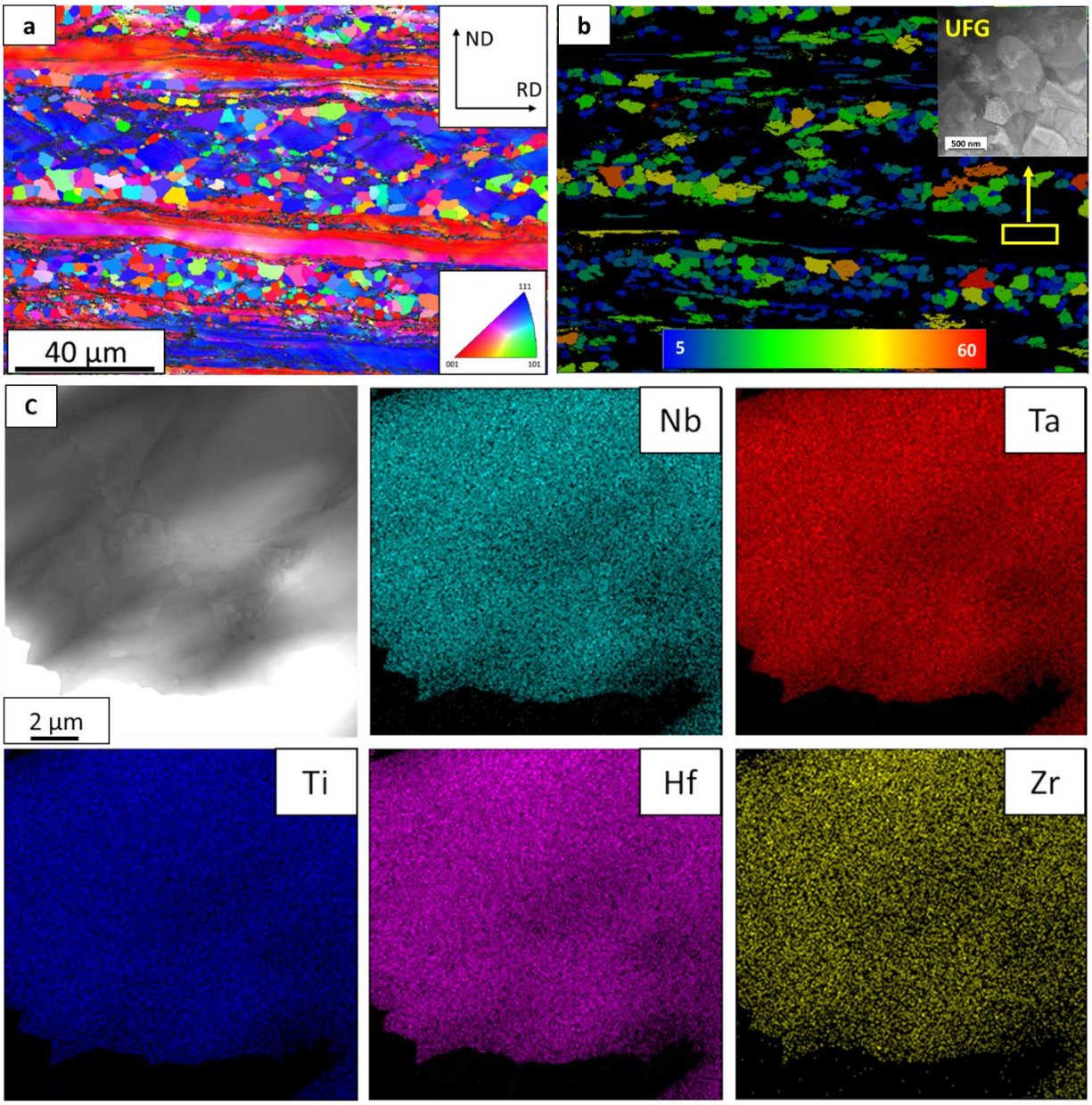

Fig. 4. Microstructure and related element distribution in $Hf_{15}Nb_{40}Ta_{25}Ti_{15}Zr_5$ RHEA with heterogeneous lamella (HL) structure. (a) EBSD inverse pole figure of $Hf_{15}Nb_{40}Ta_{25}Ti_{15}Zr_5$ RHEA after cold rolling with RIT of 90% and annealing at 900°C for 1 hour. (b) Corresponding grain area map of fully-recrystallized fine grains with grain area larger than 5 μm^2. Ultrafine grains (UFGs) in the recovery state are distributed in the black areas. (c) Scanning TEM micrograph and related EDS mapping of ultrafine and fine grains in the rolled and annealed $Hf_{15}Nb_{40}Ta_{25}Ti_{15}Zr_5$, showing no element segregation. RD – rolling direction, ND – normal direction.

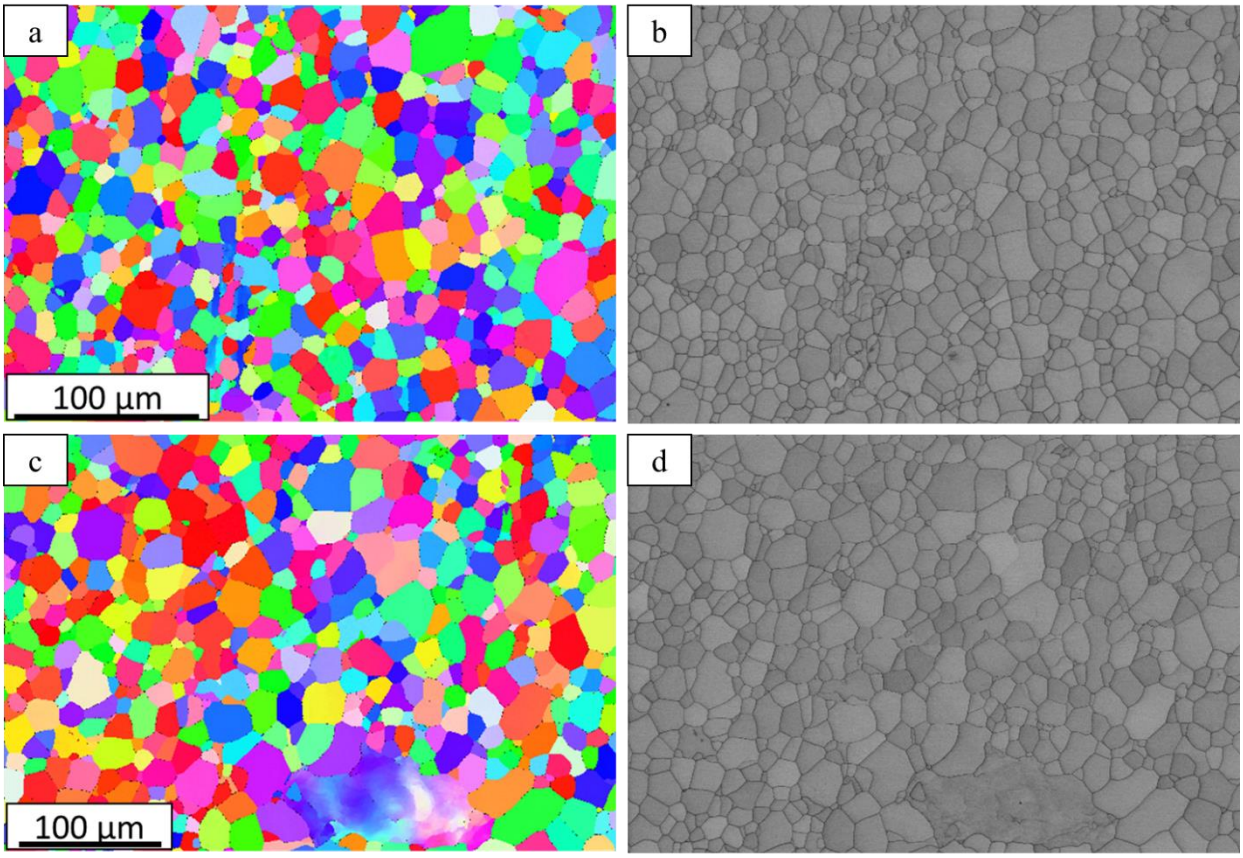

Fig. 5. EBSD inverse pole figures and related band contrast images for cold-rolled $Hf_{15}Nb_{40}Ta_{25}Ti_{15}Zr_5$ RHEA with different microstructures after annealing at different conditions. (a) EBSD IPF for CR90 $Hf_{15}Nb_{40}Ta_{25}Ti_{15}Zr_5$ RHEA after annealing at 1150°C for 1 h. (b) Related EBSD BC image for (a), showing a fine-grained microstructure. (c) EBSD IPF for CR90 $Hf_{15}Nb_{40}Ta_{25}Ti_{15}Zr_5$ RHEA after annealing at 1300°C for 0.5 h. (d) Related EBSD BC image for (c), showing a coarse-grained microstructure.

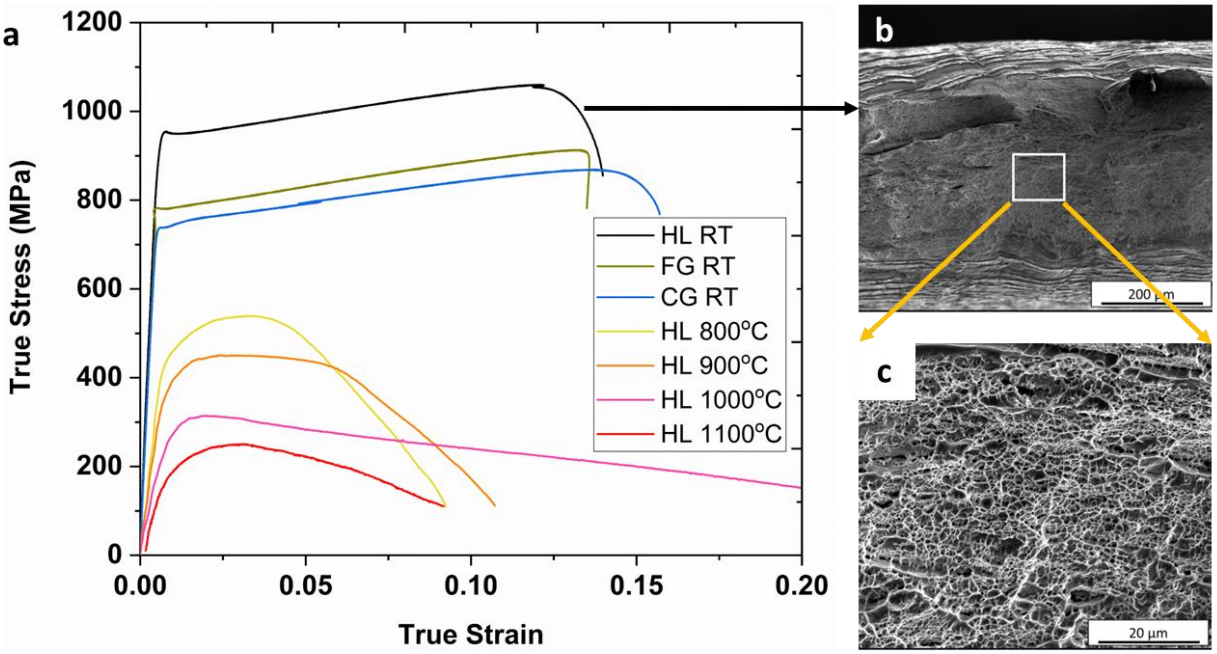

Fig. 6. High tensile strength-ductility synergy achieved in $Hf_{15}Nb_{40}Ta_{25}Ti_{15}Zr_5$ RHEA with HL structure at ambient-to-elevated temperatures. (a) Engineering stress-strain (SS) curves of $Hf_{15}Nb_{40}Ta_{25}Ti_{15}Zr_5$ RHEA with HL structure at ambient temperature and elevated temperatures (800°C, 900°C, 1000°C and 1100°C). Related SS curves of specimens with fine grains (FG) and coarse grains (CG) tested at room temperature are also shown. **SEM micrographs for the fracture surfaces of HL- NTTHZ RHEA after tensile test at room temperature**, showing a high density of dimples and ductile fracture type in (b) and (c).

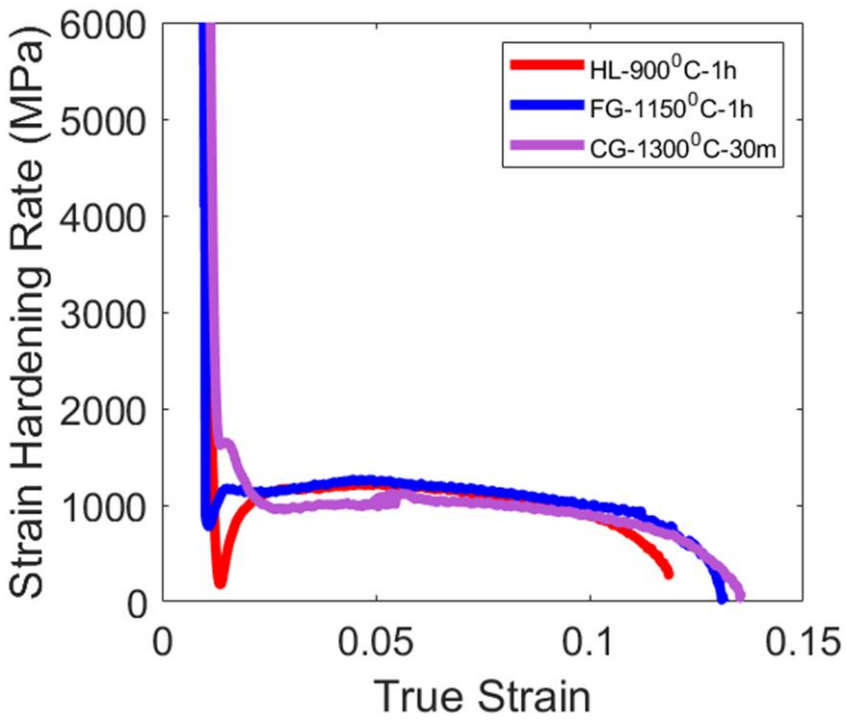

Fig. 7. Strain hardening rate curves of $Hf_{15}Nb_{40}Ta_{25}Ti_{15}Zr_5$ RHEA with different microstructures tested at room temperature.

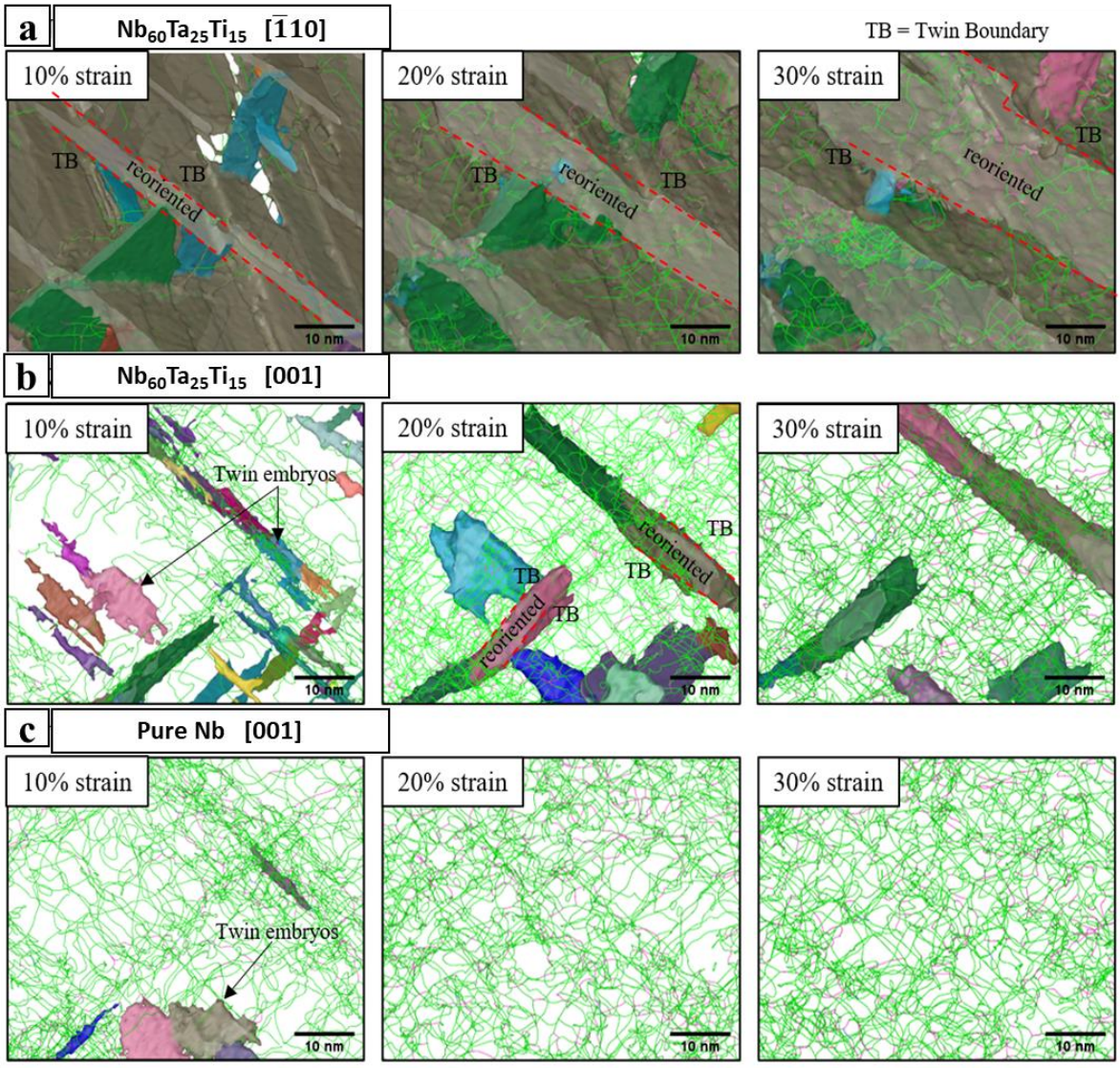

Fig. 8. Structural evolution response to compression. (a) $Nb_{60}Ta_{25}Ti_{15}$ under compression along [$\bar{1}$10] direction at 10% strain, 20% strain, 30% strain respectively. From left to right, nucleation of twin embryos, twin propagation, and twin growth to span the simulation volume. (b) $Nb_{60}Ta_{25}Ti_{15}$ under compression along [001] direction. Twin embryos and twin growth within $Nb_{60}Ta_{25}Ti_{15}$. (c) pure Nb under compression along [001] direction, deformation governed by pure dislocation slip. Dislocations appear as green and magenta lines. The twins appear as surface mesh. Different colors represent different lattice orientations generated by grain segmentation algorithm in OVITO.

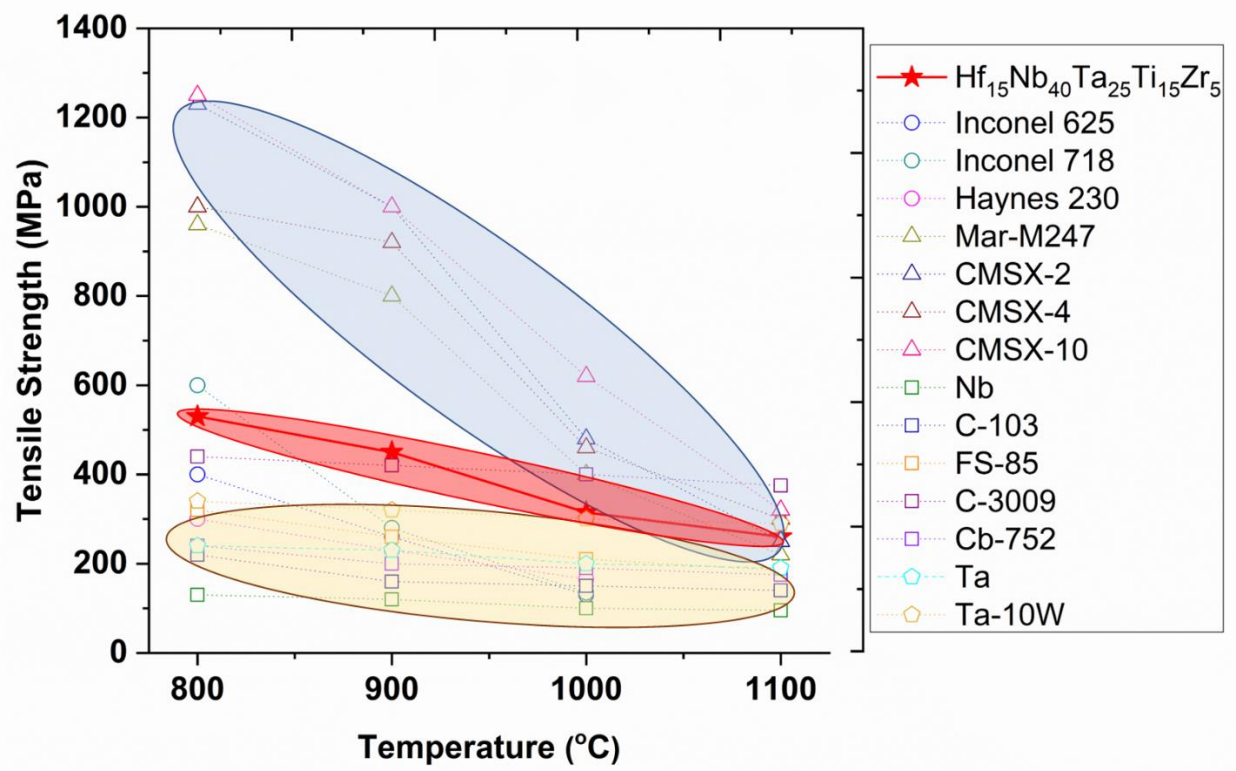

Fig. 9. Tensile strength versus the testing temperatures of $Hf_{15}Nb_{40}Ta_{25}Ti_{15}Zr_5$ with HL structure compared with those of ductile high-temperature metals and alloys, including conventional Ni-based superalloys [60-65], refractory metals (Nb, Ta) [61], and refractory Nb-based alloys and Ta-based alloys [61,66]. Blue and yellow shadow is for the strength range of superalloys (blade use) and refractory metallic materials at elevated temperatures, respectively.

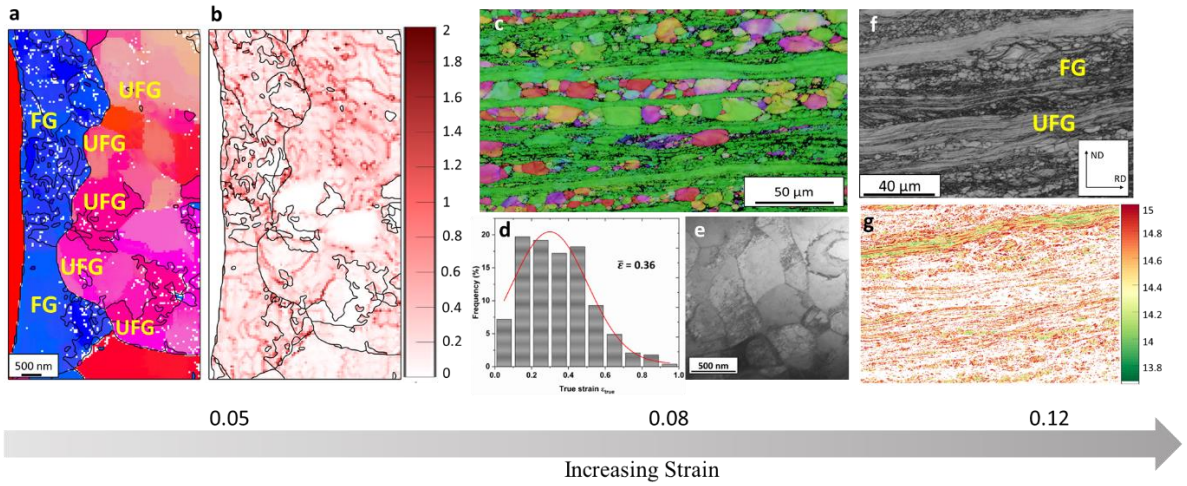

Fig. 10. Deformation mechanisms of $Hf_{15}Nb_{40}Ta_{25}Ti_{15}Zr_5$ RHEA with HL structure at different plastic stages. (a) TEM precession electron diffraction (PED) IPF for deformed $Hf_{15}Nb_{40}Ta_{25}Ti_{15}Zr_5$ RHEA with strain of 0.05. (b) Corresponding kernel average misorientation map (KAM) taken from the deformed specimen in (a), showing a higher strain localization and stronger dislocation activities along interfaces, unit: degree; (c) EBSD IPF image showing most fine grains are elongated along tensile direction at a strain of 0.08; (d) Distribution of strains in fine grains with an average true strain of 0.36 when the HL specimen is deformed to a strain of 0.08; (e) TEM micrograph showing equiaxed ultrafine grains in the HL specimen with a strain of 0.08; (f) EBSD band contrast (BC) micrograph of $Hf_{15}Nb_{40}Ta_{25}Ti_{15}Zr_5$ with strain of 0.12. (g) EBSD-based grain average GND density map corresponding to (D), showing a significant heterogeneous distribution of dislocation density, unit: $\log_{10}(m^{-2})$.

Graphical Abstract

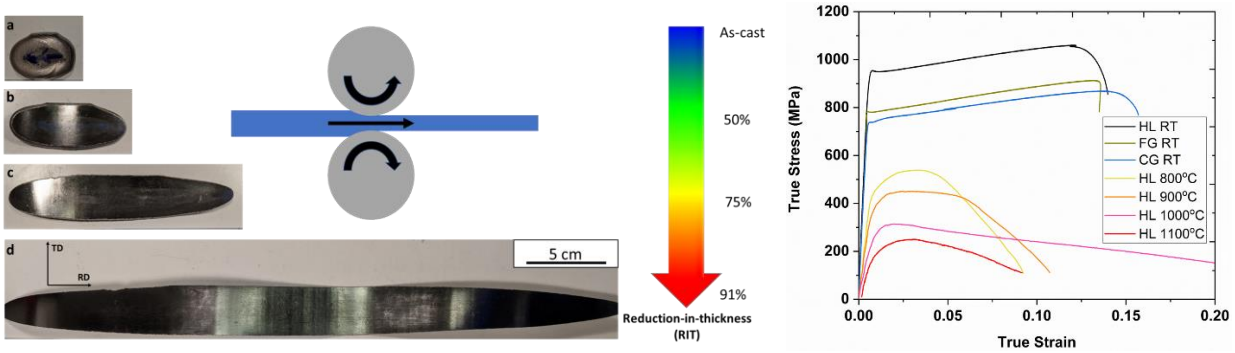

As-cast $Hf_{15}Nb_{40}Ta_{25}Ti_{15}Zr_5$ RHEA can be cold-rolled to a reduction in thickness of over 90% without surface treatment and intermediate annealing, showing excellent formability. Moreover, this RHEA is both strong and ductile at cryogenic-to-elevated temperatures.

Declaration of interests

☒ The authors declare that they have no known competing financial interests or personal relationships that could have appeared to influence the work reported in this paper.

☐The authors declare the following financial interests/personal relationships which may be considered as potential competing interests: